Numerical modeling of passive electroseismic surveying

Fabio I Zyserman, L B Monachesi, A H Thompson, L Jouniaux, P Gauzellino, T d'Biassi

submitted to *Geophys. J. Int.*

Numerical modeling of passive electroseismic surveying

F. I. Zyserman[1,3], L. B. Monachesi[2,3], A. H. Thompson[4], L. Jouniaux[5], P. Gauzellino[1], T. D'Biassi[6]

[1] *Facultad de Ciencias Astronómicas y Geofísicas, Universidad Nacional de La Plata*

Paseo del Bosque s/n, B1900FWA La Plata, Argentina

[2] *Instituto de Investigación en Paleobiología y Geología, Universidad Nacional de Río Negro*

Av. Roca 1242, Gral. Roca, Río Negro, Argentina

[3] *CONICET, Argentina*

[4] *Independent Researcher*

[5] *Université de Strasbourg, CNRS, Institut Terre et Environnement de Strasbourg UMR7063,*

[6] *YPF S.A., Argentina*

SUMMARY

This work reports numerical modeling of electroseismic conversions when the electric field source originates in the atmosphere. Random conductivity inhomogeneities in the subsurface rotate electric fields from transverse-electric to transverse-magnetic galvanic currents. Layered structures of conductivity anomalies yield rotated electric fields at reservoir depths as large as source fields at the surface. Active-source electroseismic field tests imaged reservoirs 1800 meters deep. However, the required high-power, dipole sources mediate against these methods finding practical application in hydrocarbon exploration. We extend previous research by considering the potential for using environmental electric fields to create useful electroseismic conversions. World-wide lightning strikes induce time-dependent electric fields in the atmosphere. In the frequency band appropriate for seismic surveying, 1 to 100 Hz, electromagnetic field pulses occur at a rate of 10 to 100 pulses per second. These

pulses create horizontal electric fields in the earth's surface that induce transverse-electric currents. Those currents preferentially channel through high-conductivity layers. Charge accumulates at the termini of conducting layers. That charge accumulation induces galvanic currents. Vertical galvanic currents propagate to depth where they generate propagating seismic waves at gradients in electrical properties, such as conductivity gradients at reservoirs. We use 2D numerical simulations on three different, layered-earth models to estimate the seismic amplitudes generated by passive fields. High-conductivity anomalies above a reservoir rotate the source TE fields to galvanic, TM fields. The modeling shows that the mode-rotated fields can induce potentially-useful vertical electric fields at depth. The generated seismic amplitudes at the top of the reservoir are sensitive to the oil content of the reservoir, the frequency of the primary electric field, the geometry of the conducting layers, and various material properties. Finally, a hypotetical laterally complex reservoir configuration was tested which confirms the mentioned results and aditionally shows the ability of the proposed method to delineate water-oil contacts.

1 INTRODUCTION

Seismic prospecting is the standard for hydrocarbon exploration because of its high spatial resolution, combined with decades of development and understanding. However, seismic waves are not particularly sensitive to the presence of hydrocarbon. Great skill and interpretation of data are required to gain insight into the likelihood of finding useful accumulations. On land, seismic prospecting is expensive, requires substantial equipment, and extensive workforce to complete a survey. Seismic sources disrupt the environment, interfere with infrastructure, and disrupt human activities. Particularly on land, a benign survey method that is sensitive to hydrocarbon detection will advance exploration and production.

Although coupling between electromagnetic and seismic energies has been discussed since the 1930's (Thompson 1936), successful field-tests of seismoelectric conversion date to Martner and Sparks (1959). They detected the depth of the weathered zone using seismic charges at various depths and grounded dipoles on the surface. Subsequently, several research studies attempted to image shallow targets. There are excellent review articles covering the extensive literature after 1959 (Jouniaux and Zyserman 2016). Thompson and Gist (1993) published seismoelectric and electroseismic studies that

detected gas sands to depths of 300 m. They used weight-drop seismic sources and audio power amplifiers for sources. In the following year, Pride (1994) published the seminal paper on the theory of electrokinetic coupling. Haartsen and Pride (1997) addressed the problem of seismoelectric waves generated from point seismic sources and interfacial conversions. In seismoelectric surveying, seismic waves generated on the surface create seismoelectric conversions at subsurface targets. At interfaces in elastic properties, pressure gradients create discontinuous changes in the local electric fields that generate propagating electromagnetic modulations. No radiation from seismic pressure gradients occurs in a homogeneous medium (Gershenzon et al. 2014; Pride 1994). Thompson and coworkers developed methods for reservoir-scale electroseismic surveying with high-power electrical sources (Thompson et al. 2007; Hornbostel and Thompson 2007). They concluded that electroseismic surveying is energetically more practical than seismoelectric surveying for hydrocarbon exploration and imaged reservoirs to depths of 1800 m. Coded waveforms (Hornbostel and Thompson 2007) and many repetitions were required because the signal amplitude is small. Measurements in wells and other supplementary measurements confirmed generation of electroseismic conversions at the reservoir and propagation of the seismic wave to the surface. The studies of active-source electroseismic conversions showed that conversion occurs in the transition zone between the hydrocarbon and aquifer, not at the top of the lithological structure housing the reservoir. The most easily-detected signal was second order; i.e., the detected signal occurs at double the frequency of the source signal.

In the last years a lot of effort was put on the development of the seismoelectric method, the reciprocal to electroseismic method, as a potential prospecting tool. Several authors have focused on a wide variety of aspects by means of theoretical developments and through field and laboratory tests. Among the latter Peng et al. (2017) studied the effect of the geometry of different sandstone samples in the interface response and Peng et al. (2020), carried out seismoelectric measurements on shales together with some comparative measurements on sandstones. Their experimental results showed that the amplitudes of the seismoelectric coupling coefficient in shales are comparable to that exhibited by sandstones, and are approximately independent of frequency in the seismic frequency range. Butler et al. (2018) carried out a field trial of seismoelectric surveying, in which they were able to identify a quasi-coseismic signal characterized in theoretical studies (Ren et al. 2016, 2018) as evanescent electromagnetic waves. Wang et al. (2020b) recorded the coseismic electric and interface signal while performing laboratory seismoelectric measurements mimicking marine exploration. The amplitudes of the signals were in the order of tens to hundreds of microvolts, wherefrom the authors suggested that seismoelectrics could be a potential tool to study the soil structure beneath the seafloor. Wang et al. (2021) performed laboratory seismoelectric logging while drilling (LWD) tests in a scaled borehole model. The seismoelectric signals induced by so called collar waves were too weak to be

distinguished in the full waveforms of seismoelectric LWD measurements; on the other hand, the formation P- and S-wave velocities were detected accurately from the recorded seismoelectric LWD data. Devi et al. (2018) performed a series of lab experiments, based on previous theoretical studies (Dietrich et al. 2018), where they demonstrated that multielectrode arrays could be useful to enhance the electromagnetic interface response. Dzieran et al. (2019) introduced seismoelectric spectral ratios (SESRs) as a tool to study the influence of IRs on the overall measured SE signal independently of the source time function. They applied the technique to data induced by an earthquake and showed that the SESRs displayed a site specific frequency dependence caused by IRs excited some hundreds of meters underneath the recording stations. With regard to recent theoretical developments, for an extensive account in this topic and also on field and laboratory studies the reader is referred to the review of Jouniaux and Zyserman (2016), or the book edited by Grobbe et al. (2020). We mention here some work among the large number of them in this area. Dzieran et al. (2020) employed the SESRs to numerically study the feasability to monitor changes of hydrological parameters in near surface aquifers in seismically active regions. Wang et al. (2020a) performed a thorough analysis of all conversions both in seismoelectrics and electroseismics employing semi-analytic solutions of Pride's equations with point sources in a marine stratified model. Concerning conversions induced by pure shear horizontal waves Zyserman et al. (2017a,b) studied conversions induced in the vadose zone, analyzing their dependence on soil characteristics, while Wang et al. (2020c) analyzed this problem considering a borehole setup and corresponding semi-analytic solutions previously obtained by one of the authors. Monachesi et al. (2018a,b) developed analytic solutions to seismoelectric conversions in the vadose zone and for a glacier overlying a rocky bed respectively. Gao et al. (2019) presented a frequency domain finite difference method to solve the two dimensional SHTE problem.

Background for passive electroseismic method

Most of the aforementioned studies are focused on the active-source problem. However, as mentioned, a method that uses natural sources of energy would constitute a more benign and significantly less expensive technique. The electric field from world-wide lightning is studied in depth for several practical reasons, including safety and electrical infrastructure security. The lightning pulses occur at a rate of 10 to 100 pulses per second. Near a single lightning source, the induced electromagnetic pulses are typically hundreds of microseconds wide. After averaging over a large number of strikes traveling long distances (typically in the order of hundreds of km) horizontally through the near surface, the lightning pulses form a Gaussian distribution that is useful for imaging purposes (Raab 2010). The amplitude of the Gaussian waveform ranges from 1 μV/m to 1 mV/m. The electric fields are typically vertical and the magnetic fields horizontal near a lightning strike. The horizontal oscillation of the magnetic field is orthogonal to the direction to the lightning source. At any particular location, far

removed from the lightning source, electromagnetic noise is composed of impulsive and random, Gaussian noise components. The impulsive components originate in lightning discharges and noise pulses close to the test site. The Gaussian component is the sum of more-distant lightning and other random noise (Raab 2010). All the parameters are time-dependent. For example, there are systematic diurnal variations. Rakov and Uman (2003) provide a thorough overview of lightning.

To the authors' knowledge, the theoretical study of the potential application of the passive electroseismic method as a new prospecting tool was not addressed before. In the present study we perform numerical simulations of electroseismic conversions induced by natural electromagnetic sources. By designing different subsurface models we analyze the effects of the different petrophysical and electrical parameters of the models and the ability of the method in delineating the main characteristics of a target hydrocarbon reservoir. That is, we want to answer whether ES signals from natural electromagnetic sources can be observed and how reservoir properties can be quantified from the converted ES signals. Although our studies are focused on hydrocarbon exploration, the proposed numerical methodology can be performed in a variety of prospecting scenarios.

2 THEORETICAL BACKGROUND

We describe in this section the rock physics models and governing equations we employ in our numerical procedure.

2.1 Effective model parameters

We consider two different materials building the solid matrix, namely sand and clay, and we call β_{sand} and β_{clay} their respective volume fractions; $\beta_{\text{sand}}+\beta_{\text{clay}}=1$. The values of these fractions, for each one of the regions in the employed models are given in Table 1. The mass density of the aggregate, ρ_s, is given by the volume weighted mean of the respective components mass densities,

$$\rho_s = \beta_{\text{sand}}\ \rho_{s,\text{sand}} + \beta_{\text{clay}}\ \rho_{s,\text{clay}}. \tag{1}$$

We estimate the absolute permeability κ_0 for each formation by using the Kozeny-Carman relation (Mavko et al. 2009)

$$\kappa_0 = B\frac{\phi^3}{(1-\phi)^2}d_k^2 \qquad \text{where} \qquad \frac{1}{d_k} = \frac{1}{r_{\text{sand}}} + \frac{1}{r_{\text{clay}}}. \tag{2}$$

Here ϕ is the porosity, B is a geometric constant (we assume $B = 0.003$ (Carcione and Picotti 2006; Castromán et al. 2020)) and r_* denote the radius of the respective particles.

For the effective shear and bulk moduli of the aggregate, G_s and K_s, we use the Reuss lower bounds (Mavko et al. 2009), calculated in terms of the components volume fractions, shear moduli and bulk

moduli respectively

$$G_s = \left(\frac{\beta_{\text{sand}}}{G_{s,\text{sand}}} + \frac{\beta_{\text{clay}}}{G_{s,\text{clay}}} \right)^{-1}, \qquad K_s = \left(\frac{\beta_{\text{sand}}}{K_{s,\text{sand}}} + \frac{\beta_{\text{clay}}}{K_{s,\text{clay}}} \right)^{-1}. \tag{3}$$

In order to compute the elastic properties of the rock formations, that is, of the porous matrix, we employ two different approaches. For the most superficial, unconsolidated layers as in Pride (2005); Bordes et al. (2015); Dupuy et al. (2016); Zyserman et al. (2017a); Monachesi et al. (2018b) we use Walton model (Mavko et al. 2009) to obtain their shear modulus G and bulk modulus K

$$G = \frac{1}{10} \left[\frac{3(1-\phi)^2 \hat{C}^2 P}{\pi B^2} \right]^{\frac{1}{3}}; \text{with} \quad B = \frac{1}{4\pi} \left(\frac{1}{G_s} + \frac{1}{G_s + \lambda_c} \right), \qquad K = \frac{5}{3} G. \tag{4}$$

In this equation, $\hat{C}$ is the so called coordination number, and is related to the packing of the spheres building the solid aggregate in this conceptual model, P is the hydrostatic pressure and $\lambda_c = K_s - \frac{2}{3} G_s$ is Lamé's coefficient of the effective grain material. In this work we consider $\hat{C} = 9$ and $P = 101325$ Pa.

On the other hand, we characterize the elastic properties of the consolidated formations by means of a model proposed by Pride (2005)

$$G = G_s \left(\frac{1-\phi}{1 + C_s \phi} \right), \quad K = K_s \left(\frac{1-\phi}{1 + \frac{3}{2} C_s \phi} \right), \tag{5}$$

where C_s is the "consolidation parameter", which quantifies the degree of cohesion between the solid grains of the porous rock. For consolidated sandstones, it is expected that this parameter ranges from C_s=2 (extremely consolidated) to C_s=20 (poorly consolidated) depending on certain properties of the microstructure.

As Biot model's intrinsic attenuation is not able to explain the high energy loss levels of waves traveling through unconsolidated soils (Schön 1996), we consider, for the bulk material, a linear viscoelastic behavior. The latter is obtained by replacing the real bulk and shear moduli K and G by complex frequency dependent functions $K^\star(\omega)$ and $G^\star(\omega)$, where ω is the angular frequency. They are obtained using Liu et al. (1976) linear viscoelastic model, which for the shear modulus is $G^\star(\omega) = G/(R(\omega) - iT(\omega))$. The functions $R(\omega)$ and $T(\omega)$, associated with a continuous spectrum of relaxation times, characterize the viscoelastic behavior and are given by (Santos et al. 2004)

$$R(\omega) = 1 - \frac{1}{\pi \widehat{Q}} \ln \left(\frac{1 + \omega^2 T_1^2}{1 + \omega^2 T_2^2} \right), \qquad T(\omega) = \frac{2}{\pi \widehat{Q}} \tan^{-1} \left(\frac{\omega (T_1 - T_2)}{1 + \omega^2 T_1 T_2} \right).$$

The model parameters $\widehat{Q}$, T_1 and T_2 are taken such that the soil quality factor $Q(\omega)$ is approximately equal to the constant $\widehat{Q}$ within the chosen frequency range. As this work is restricted to the seismic frequency range, $T_1 = \frac{1}{2\pi} 10^6$ s and $T_2 = \frac{1}{2\pi} 10^{-7}$ s in our simulations. Although there are other models to account for the energy loss, e.g. (Chotiros and Isakson 2004; Gauzellino et al. 2014), we used Liu's

model because it provides a constant quality factor over the frequency range considered, the moduli $K^\star$ and $G^\star$ are well behaved at $\omega \to 0$ and ensures causality, which is a reasonable behavior for geophysical applications -unless otherwise expected in a particular model-, as suggested in Santos et al. (2005).

In Pride's formulation of electroseismics, a single electrolyte fully saturating the rock matrix is considered. In the models we study in this work this scenario is taken into account, together with partially saturated porous media and fully saturated porous media containing two immiscible fluids. So, in order to extend the validity of our theoretical frame it is necessary to introduce appropriate effective fluid properties. To this end, we follow here the same approach taken by Zyserman et al. (2012); Warden et al. (2013); Smeulders et al. (2014); Bordes et al. (2015); Zyserman et al. (2015); Monachesi et al. (2018a,b) as follows: For the effective fluid mass density we consider (Bordes et al. 2015)

$$\rho_f = \rho_w S_w + \rho_l (1 - S_w), \quad l = air \text{ or } oil, \tag{6}$$

where $S_w + S_l = 1$, $l = air$ or oil is assumed. Notice that we do not consider the case of the pore volume partially saturated with water and oil. The effective fluid bulk modulus is computed as the harmonic average of the fluid components (Reuss lower bound)

$$K_f = \left(\frac{S_w}{K_w} + \frac{1 - S_w}{K_l} \right)^{-1}, \quad l = air \text{ or } oil, \tag{7}$$

where K_w and K_l, $l = air$ or oil are the bulk moduli of water and air or oil respectively. The viscosity of the effective fluid is computed in terms of the mixture components viscosities and water saturation using (Teja and Rice 1981)

$$\eta = \eta_l \left(\frac{\eta_w}{\eta_l} \right)^{S_w}, \; l = air \text{ or } oil. \tag{8}$$

In this expression, η_w and η_l, $l = air$ or oil are the viscosities of water and air or oil respectively. As usual, the shear modulus of the saturated rock matrix is assumed to be equal to G, the shear modulus of the dry matrix.

We consider now the electrical conductivity of the porous medium when it is either partially saturated with water or fully saturated with water and oil. As we consider the electric conductivity of air and oil to be zero, we can in both cases use the expression proposed by Warden et al. (2013), extending Pride's original formula (Pride 1994, Eq.(242)) to the realm of partially saturated media:

$$\sigma(S_w, \omega) = \frac{S_w^{\hat{n}}}{F} \sigma_w + \frac{2}{F} \frac{C_{em} + C_{os}(\omega)}{\Lambda}. \tag{9}$$

The first term in this equation is Archie's law for a partially saturated medium, where $F = \phi^{-\hat{m}}$ stands for the formation factor, $\hat{m}$ being the cementation exponent and $\hat{n}$ the Archie's saturation

exponent. The electrical conductivity of water containing sodium chloride can be computed as $\sigma_w = \sum_{l=Na^+,Cl^-}(ez_l)^2 b_l N_l$, where $e = 1.6 \times 10^{-19}$ C is the electron electric charge, and z_l is the ions' valence, taken to be equal to 1 for both species. The ions' mobility $b_l = 3 \times 10^{11}$ N s/m, $l = Na^+, Cl^-$ and the concentration $N_l = N_a C_0$, where C_0 is the water salinity in mol/l and $N_a = 6.022 \times 10^{23}$ 1/mol is Avogadro's number (Carcione et al. 2003). The second term in Eq.(9) accounts for the surface conductivity; in it, as Pride (1994) stated, the factor C_{em} is the excess conductance associated with the electromigration of double layer ions; $C_{os}(\omega)$ is the frequency-dependent electro-osmotic conductance due to electrically induced streaming of the excess double-layer ions. We compute these conductances employing their original expressions (Pride 1994; Carcione et al. 2003; Munch and Zyserman 2016). Finally, Λ is a parameter obtained from the condition $(\xi \alpha_\infty \kappa_0)/(\phi \Lambda^2) = 1$ (Pride 1994); pore-geometry dependent factor ξ lies in the range $4 \leq \xi \leq 8$ and in this work we consider $\xi = 8$, which corresponds to a network of variable-radii tubes. Finally $\alpha_\infty = \phi F$ is the tortuosity. We remark here that, as in Brovelli et al. (2005) and Warden et al. (2013), the surface conductivity is assumed to be independent of water saturation, because under realistic saturation ranges (residual water saturation $S_{wr} \geq 0.1$) the thickness of the wetting phase layer is always larger than the Debye length, which for the considered electrolyte is $d = \sqrt{(\epsilon_w k_B T)/(2e^2 N)}$. Here ϵ_w is the water electric permittivity, k_B is the Boltzmann's constant and T the absolute temperature (so that $k_B T$ is the thermal energy). This also means that all fluid related properties involved in the calculation of the surface conductivity and of the electrokinetic coupling -see below- are just those of water. Note that another approach, with a water saturation dependent surface conductivity can also be considered; however, it can be observed that it does not affect significantly the seismoelectromagnetic conversions for the considered soils (Zyserman et al. 2017b).

For the electrokinetic coupling, when the porous medium is partially saturated with water or fully saturated with water and oil -we consider the water to be the wetting phase in both cases-, again following Warden et al. (2013); Bordes et al. (2015) we use:

$$L_0(S_w) = -\frac{\phi}{\alpha_\infty}\frac{\epsilon_w \zeta}{\eta_w}\left(1 - 2\frac{d}{\Lambda}\right) S_w^{\hat{n}} \mathcal{C}(S_w). \tag{10}$$

In this equation ζ is the zeta potential, which we compute as a function of the water salinity C_0 as $\zeta = 0.008 + 0.026 \log_{10}(C_0)$ (Pride and Morgan 1991). However, as suggested in Jaafar et al. (2009); Dzieran et al. (2020) for high salinities (above 0.2 mol/l) we set a constant $\zeta = -0.02$ V. $\mathcal{C}(S_w)$ is a function relating the streaming potential coefficient (SPC) obtained under partial saturation conditions to the one corresponding to full saturation conditions. The SPC corresponds to the electric potential difference over the pressure difference at the origin of this electrical signal. If the fluid flow does not

induce an electric signal, the SPC is zero, therefore the electrokinetic coupling L_0 is also zero, and no seismo-electromagnetic conversions are possible. For a tutorial on these effects see Jouniaux and Ishido (2012). In eq. (10), as in previous works (Zyserman et al. 2015, 2017a), we use

$$\mathcal{C}(S_w) = \left(\frac{S_w - S_{wr}}{1 - S_{wr}}\right)\left[1 + 32\left[1 - \left(\frac{S_w - S_{wr}}{1 - S_{wr}}\right)\right]^{0.4}\right], \qquad S_{wr} = 0.10. \tag{11}$$

This expression was experimentally derived from laboratory measurements of the streaming potential coefficient in partially saturated sands and displays a non monotonic dependence with water saturation (Allègre et al. 2010, 2012; Allegre et al. 2014; Allègre et al. 2015; Fiorentino et al. 2017). For water saturations below S_{wr}, $\mathcal{C}(S_w)$ is set to zero. Others different available models for $\mathcal{C}(S_w)$ have already been discussed by ourselves and other authors as well, see Perrier and Morat (2000); Allègre et al. (2010); Strahser et al. (2011); Zyserman et al. (2017a); Glover et al. (2019); Jougnot et al. (2012, 2015, 2020). In the last three references $\mathcal{C}(S_w)$ is discussed within the frame of the effective charge density approach for the electrokinetic coupling.

2.2 Governing equations

As it is usual in the seismoelectromagnetic literature, after checking that our models verify the necessary conditions, we neglect the electrofiltration feedback, which allows us decouple the electromagnetic response from the seismic one. Therefore we compute the electromagnetic fields in a first stage by solving Maxwell's equations, and their induced seismic response afterwards, by solving Biot's equations.

2.2.1 Maxwell's equations

We consider as the source of our numerical experiment plane electromagnetic waves with components E_x and H_y impinging normally to the Earth's surface as it is usually considered in magnetotelluric studies (Ward and Hohmann 1987; Simpson and Bahr 2005); meanwhile, as depicted in Fig.1, we choose a two dimensional geometry for the subsurface.

We want to compute the total electromagnetic fields $\mathbf{E}$ and $\mathbf{H}$ in our region of interest, considering that the electric conductivity of the subsurface is given by

$$\sigma = \begin{cases} \sigma^p(z) & \text{layers,} \\ \sigma^p(z) + \sigma^s(x,z) & \text{inhomogeneities,} \end{cases} \tag{12}$$

where "p" and "s" stand for *primary* and *secondary*, respectively. Writing them as $\mathbf{E} = \mathbf{E}^p + \mathbf{E}^s$ and $\mathbf{H} = \mathbf{H}^p + \mathbf{H}^s$ -where the explicit dependence on coordinates (x, z) and angular frequency ω has been neglected for the sake of simplicity- it can be seen that on one hand $\mathbf{E}^p = (E_x^p, 0, E_z^p)$, $\mathbf{H}^p = (0, H_y^p, 0)$

are solution to

$$\partial_z E_x^p - \partial_x E_z^p + i\omega\mu_0 H_y^p = 0, \tag{13}$$

$$\sigma^p(E_x^p, E_z^p) - \left(-\partial_z H_y^p, \partial_x H_y^p\right) = 0. \tag{14}$$

In this setting the incident wave has amplitudes E_x^0 and H_y^0 for the electric and magnetic fields respectively at the surface of the Earth. It is well known that under these assumptions, considering a layered conductivity structure, and that the fields decay to zero as $z \to \pm\infty$, the so called primary fields can be analytically computed, and do not have a vertical component. On the other hand, the secondary fields are solutions to

$$\partial_z E_x^s - \partial_x E_z^s + i\omega\mu_0 H_y^s = 0, \tag{15}$$

$$\sigma(E_x^s, E_z^s) - \left(-\partial_z H_y^s, \partial_x H_y^s\right) = \sigma^s(E_x^p, 0), \tag{16}$$

plus appropriate boundary conditions on the computational borders; we employ absorbing boundary conditions (ABCs) on them (Zyserman et al. 2010, 2012; Santos et al. 2012; Manassero et al. 2020). Eq.(16) together with the ABC's have to be solved numerically, task we perform by means of our own finite elements code (Zyserman et al. 2010).

2.2.2 Biot's equations with electrokinetic source

In terms of the solid matrix displacements u^s and relative fluid displacements u^f, the wave equations in the poroelastic media are

$$-\omega^2\rho_b(u_x^s, u_z^s) - \omega^2\rho_f(u_x^f, u_z^f) - \nabla\cdot\tau = (0,0), \tag{17}$$

$$-\omega^2\rho_f(u_x^s, u_z^s) - \omega^2 g_0(u_x^f, u_z^f) + i\omega\frac{\eta}{\kappa_0}(u_x^f, u_z^f) + \nabla p_f = \frac{\eta}{\kappa_0}L_0(S_w)(E_x, E_z). \tag{18}$$

Here, ∇ in the first (second) equation stands for the two dimensional divergence (gradient). The stress tensor $\tau_{ij} = 2G\varepsilon_{ij}(u^s) + \delta_{ij}\left(\widehat{\lambda}_c\nabla\cdot u^s + \alpha K_{av}\nabla\cdot u^f\right)$, with $i,j = x,z$. In this expression, $K_{av} = ((\alpha-\phi)/K_s + \phi/K_f)^{-1}$, $\alpha = 1 - K/K_s$ and $\widehat{\lambda}_c = K_c - \frac{2}{3}G$, with $K_c = K + \alpha^2 K_{av}$ being the bulk modulus of the fluid saturated rock matrix. In Eq. (17) the bulk density ρ_b is computed as usual $\rho_b = \phi\rho_f + (1-\phi)\rho_s$, and in Eq.(18), $g_0 = \frac{3}{2}\alpha_\infty/\phi$ is the so called inertial coupling and the pressure $p_f = -\alpha K_{av}\nabla\cdot u^s - K_{av}\nabla\cdot u^f$. We equip Eqs.(17)-(18) with a set of ABC's, and compute numerical solutions to them by means of an already presented finite element algorithm (Zyserman et al. 2010, 2012; Santos et al. 2012).

3 LAYOUT

Our study is focused on the potential application of the passive electroseismic method in a hydrocarbon exploration setting. We consider three different models with an oil reservoir at 500 m depth (Fig.1). They share the same layered structure and properties, but differ in the number and geometry of the considered conductive anomalies, immersed in one of the common layers. The two uppermost layers (1 and 2) are considered to form a poorly consolidated anelastic soil with high porosity and relatively low electric conductivity, which in turn gives these uppermost layers a markedly low seismic velocity. These layers overlay a lossless sandstone (layer 3) with lower porosity and electric conductivity. In this layer, laterally extended horizontal electrically conductive structures (henceforth referred to as *slabs*) are set, with different mechanical properties than the host layer (layer 3). Finally, the fourth and deepest layer, depicting the characteristics of an oil reservoir, is also a relatively porous lossless sandstone with a very low electric conductivity. This layer is partially saturated with oil and water, whilst the three overlying layers, and the slabs, are fully saturated with water, with diverse salinity values. The most relevant emerging properties of all layers and slabs are displayed in Table 3. They are derived from the basic parameters displayed in Table 2 and Table 1 employing the rock physics model equations presented in Section 2.1.

As we are interested in computing the passive electroseismic response of our Earth models both in the frequency and time domains, for the former we consider that the impinging wave is monochromatic, while for the latter we consider it has the signature of a Ricker wavelet with a central frequency of 120 Hz, and a delay of 8.6 ms. We present below i) the results of the electromagnetic responses, specially the electric field at the top of the reservoir; ii) the results of the electroseismic responses, in particular the vertical seismic acceleration created at the top of the reservoir and the induced one at the surface.

4 RESULTS

4.1 Electromagnetic responses

As a first step we analize the electromagnetic response of the different models to an impinging monochromatic plane electromagnetic wave with a frequency of 0.01 Hz and unit amplitude at the surface; the goal is to determine the behavior of the electric field, and how the different conductive structures modify it, particularly, its amplitude at the top of the reservoir. Our interest is focused here because the interface response (IR) taking place at this boundary and consequently the induced seismic waves travelling from here upwards strongly depend on the electric field, as can be observed in Eq. (18). We expand in this point below, after we have completed the proposed task.

Let us look upon the top left panel of Fig. 2, in which the horizontal electric field E_x of Model

#1 in the whole region of interest is depicted. It can be observed that the conductive slab produces a decrease in the amplitude of E_x in the inner side of both vertical boundaries of the slab, and an increase on their outer side. The current density induced by the primary field E_x^0 is continuous at these vertical edges, and due to the electric conductivity jump across them, E_x is discontinuous. Moreover, the discontinuity in electrical conductivity forces charges to pile-up at both sides of these boundaries (Zhdanov 2009). This, in turn, creates a secondary electromagnetic field with both horizontal and vertical components, with a dipole-like spatial distribution. The depicted E_x field results naturally from the superposition of the described effects plus inductive ones, that is, the rotational electric field created by the time variation of the magnetic field generated by the electric currents induced by the primary electric field, but they contribute more weakly to the final result. What we can here stress is that the charge accumulation does create a vertical component of the electric field E_z, as can be seen in the top right panel of the figure. In the earth, the largest amplitudes in absolute value are observed precisely at the slab corners. Moreover, the conductivity contrast existing at the top of the reservoir is shown more clearly through E_z, than through E_x. This is natural, because the latter is continuous at this border, contrary to the former.

It can be observed that the resulting electric field amplitude is stronger when the number of conductive anomalies grows, as can be seen comparing the responses of Model #2 and Model #3 for both the horizontal and vertical components of the electric field with the results we have just discussed. Although from these pictures it is not unequivocally discernible the exact position of the maxima, for E_x the highest value is about 2.2 V/m for Model #1, above 3 V/m for Model #2 and above 6 V/m for Model #3. E_z, on the other hand, depicts highest values just above 1 V/m for the first model considered, above 2 V/m for Model #2 and above 5 V/m for Model #3. Notice, however, that if the number of slabs was further increased, at some point E_z will start diminishing until becoming zero when the layer overlying the reservoir becomes an homogeneous one; in the present case, with an electric conductivity equal to that of the slabs.

We now show in Fig.3 both components E_x (left panels) and E_z (right panels) measured at 500 m depth, along a horizontal line parallel to the reservoir top. Both top panels correspond to the frequency of 0.01 Hz, the ones below them to a frequency of 120 Hz. As we observed above, Model #3 is the one generating the largest responses, followed by those of Model #2 and Model #1 in decreasing order. All curves display a behavior consistent with the geometry of the models; the periodicity of those corresponding to Model #2 and Model #3 is apparent. On the other hand, the curves associated with the responses of Model #1 display the effect of the presence of the slab: E_x takes lower values below the conductive structure, while E_z shows the effect of its vertical edges. At the chosen depth E_x is up to almost 2.6 (36) times larger than the primary field at the surface for the lower (higher) frequency

, while E_z reaches up to near 0.8 (14) times the amplitude of the incident wave for the lower (higher) frequency, of course, in the orthogonal direction. This is remarkable; the sole presence of geological structures that can be represented by horizontal conductive slabs gives rise to a vertical component of the electric field, at the measured position, of similar magnitude as the one of the primary field. We deem the fact that for a frequency higher than those typical in magnetotellurics the responses generated by the slabs taking values so large is not trivial. Considering just the layered structure of the models, the primary field decays less than 1% at 1000 m depth at 0.01 Hz, while it preserves -at the same depth- around 90% of its original amplitude at 120 Hz. Therefore, the amplitude of the vertical electric field observed near the reservoir top depend not only on the number of slabs considered and their spatial distribution, but also on the dependence with frequency of the charge accumulation at the edges of the slabs. This fact can be observed in Fig. 4, where we plot, considering Model #3, the maximum amplitude of both E_x and E_z along $z = 500$ m depth vs frequency. Both curves depict the same behaviour, increasing from the lower frequencies up to a maximum -which E_x reaches at about 85 Hz and E_z at about 52 Hz- and decreasing monotonically from there to the end of the considered interval. So, not only the penetration depth, larger for lower frequencies, is governing the frequency response of the electric field. This situation suggests that there is a non trivial dependence of the total electromagnetic field with the general model characteristics. Indeed, the absolute value and position of the field maxima surely depend on the overall subsurface conductivity structure, involving also thicknesses of the layers, and size, shape, number and positions of the conductive slabs. However this analysis is beyond the scope of the present manuscript.

Our numerical procedure is written in the frequency domain; to compute the response in the time domain, we Fourier transform the source and compute the responses to its spectrum for a fixed number of frequencies. For each frequency, the fields are obtained in two stages: a) The electromagnetic response of the model is computed. b) The resulting electric field is used as a source for the electroseismic response of the medium. In this stage Pride's formulation is employed to consider the coupling between electromagnetic and seismic fields. Once the fields for all frequencies are available, we inverse Fourier transform them into the time domain.

In Fig.5 we display the vertical recording at the well of the electric field components, E_x (top panel), E_z (bottom panel), considering Model #1. We are neglecting the displacement currents in Maxwell's equations, so there is no electromagnetic wave propagation, but signal diffusion (Løseth et al. 2006). The signal is large enough for all receivers in the well to record the signal simultaneously. We consider that the characteristic time of the problem is determined by the time the seismic waves take to travel across the models. E_x displays a more or less constant behavior along the length of the well, with the exception of an amplitude decrease in the receivers located around the depth where the conductive

slab is located. Notice that the well traverses the conductive slab relatively near one of its edges, so the observed decay is compatible with the behavior described for this field component in Fig.2. On the other hand, correspondingly with what we have described, E_z shows a more variable behavior. Following the line of receivers from the top to the bottom of the well, those located within the two poorly consolidated layers record a relatively small field. This is consistent with their higher electric conductivity compared to the underlying layer (see Table 3). The amplitude of E_z increases as the receivers get closer to the slab, but there its amplitude is negligible, due to the large conductivity of the former. Below the conductive slab the signal inverts its polarity, and the amplitude diminishes with the distance to the receivers. This effect is not so clearly observed for the other field component. E_z is relatively large in receivers located within the more resistive, deepest layer. As expected, the normal component of the electric field is discontinuous across the reservoir top, and its amplitude is smaller in the more conductive region. In summary, E_z is generated at the vertical edges of the conductive slab and is recorded all along the length of the well, showing a behaviour compatible with the given conductivity distribution.

4.2 Electroseismic responses

4.2.1 Model #1

We turn now our attention to the responses arising from the electromagnetic-to-seismic conversions. Fig.6 depicts an important result of this work. The seismic waves having a vertical component -we display the z-component of the acceleration- originate at the reservoir top. For the sake of brevity, we analyze this result considering Model #1, the other two models displayed vertical recordings with the same characteristics. Two different kinds of waves can be observed; one of them, which we refer to as EM-coseismic waves (Zhu et al. 2008), is detected by all the receivers in the well (almost) simultaneously. These waves are induced, through the electro-osmotic phenomenon (Haines and Pride 2006), by the vertical component of the total magnetotelluric field. On the other hand, the upwards traveling wave is the fast P wave. In the embedded figure we display two traces corresponding to two recorders located in the well 102 m apart. The lapse between the positive peak of both traces is about Δt=0.0269 s, so the wave travels at about 3790 m/s. This is consistent with the velocity of the fast P wave computed from Biot's dispersion relations (Zyserman and Santos 2007; Corredor et al. 2014) that yield, for the source peak frequency (120 Hz), a velocity of 3757 m/s (see Table 3). As expected, the vertical component of the seismic wave is reflected and refracted at the deepest interface of the low consolidated layers. The reflection travels downwards at the same velocity. The transmitted wave travels slower, and reaches the surface at about 0.15 s.

We also recorded the seismic waves arriving to the surface by an array of one hundred equally

separated accelerometers set along 1600 m; the leftmost and rightmost ones are beyond the horizontal position of the respective borders of the underlying conductive slab in Model #1. In Fig. 7 two horizontal wavefronts can be clearly identified. Notice that in this figure no transformation is exerted on the recordings, the relative amplitudes are those yielded by the numerical simulation. The strongest one, located at about 0.15 s is the simultaneous arrival to all receivers of the fast P-wave originated at the reservoir top. The signal is weaker in the region around the center of the conductive slab. In Fig.3 it can be observed that E_z, near the reservoir top, that is, at 500 m depth, is almost zero at the horizontal position around the midpoint of the conductive slab, while it takes its maximum absolute value near its vertical edges. Consistently the interface response, created along the horizontal top boundary of the reservoir, is strong where the vertical electric field is strong, and weak where it is weak. The seismic waves change their polarization at $x = 0$. This is consistent with the corresponding change in sign displayed by E_z at the edges of the horizontal slab. The second arrival simultaneously recorded by all receivers takes place at about 0.33 s. This time is compatible with the arrival of an SV-wave created simultaneously with the fast P-wave at the reservoir top. As mentioned e.g. by (White and Zhou 2006), the P-wave is generated by the higher pressure in the resistive side of the interface and the SV-wave by the portion of the electric field that is not normal to the interface.

The amplitude of the vertical acceleration of the SV-wave is not as big as the one of the P-wave. However, the variation of its amplitude along the reservoir top follows a similar pattern as that of the P-wave; it is weaker in the center of the analyzed domain, and stronger towards the borders.

To explore the possibility of detecting changes in oil content in the reservoir by measuring the electroseismic response at the surface, we considered in the model three different oil saturations, 15%, 40% and 90%. In Fig.8 we depict, for each one of these saturations, the stacked squared velocity traces registered by all one hundred receivers on the surface. In this way, we get the energy density of the seismic waves arriving to the surface as a function of time independently of the receiver position. We normalize the energy density by dividing the result by the number of receivers. In the left panel of the figure the energy density of the z-component of the seismic waves is depicted, while the right one corresponds to the x-component. It is clear that the energy density is higher for both seismic wave components when the reservoir has a saturation of 40% oil. This can be partially related to the way in which the electrokinetic coefficient L_0 depends on water saturation S_w, Eqs. (10) and (11). This is an increasing function of S_w up to $S_w \simeq 0.6$; it decreases if the water saturation further increases. Consequently, as the oil and water saturations verify that $S_w + S_{oil} = 1$, it is increasing for oil saturations up to $\simeq 0.4$, and decreases for higher ones. Parameters other than $L_0(S_w)$ play a role in the genesis of the seismic interface response at the reservoir top (Garambois et al. 2002; Jouniaux and Zyserman 2016; Rosas-Carbajal et al. 2020; Zyserman et al. 2020). In this case, as we are varying just

the oil saturation, there is only one more parameter involved, which is the electric conductivity in the reservoir. The electric conductivity, as can be seen in Eq.(9) depends on the water and oil content of the formation. Another feature we can point out from Fig.8 is that the z-component of the seismic signal carries more energy than the x-component; the former presents peaks of up to 10^{-20} J/kg, while the maxima of the latter are around 10^{-24} J/kg, four orders of magnitude smaller. This is interesting, because it means that recorders set at the surface will more easily -or with less difficulty- detect the z-component of the seismic signal. The z-component presents another remarkable attribute; for all the considered saturations clearly distinguishable peaks at about 0.15 s and 0.33 s are observed. These peaks are associated with the arrival of the P and SV waves to the surface. In all three cases the first ones are higher than the second ones, being those with $S_{oil} = 0.4$ the strongest. On the contrary, the curves associated with the x-component do not show any clear response associated to the SV waves. However, the peaks associated with the P wave are present, but they have similar amplitude for all saturations, and they are not as sharp as the ones of the z-component.

As a summary of this analysis, we remark that the z-component of the seismic wave acceleration induced by an electroseismic conversion at the reservoir top can be detected on the surface, and that this signal is sensitive to the oil saturation.

4.2.2 All models

We next compare the differences in the seismic responses measured on the surface in Models #1, #2 and #3. In this analysis, considering the previous results, we set the oil saturation of the reservoir $S_{oil} = 0.4$, so that the strongest response of Model #1 is selected. Moreover, following the analysis we did above, we consider now just the z-component of the acceleration. We start by considering the traces recorded at the well position, for all models; they are depicted in Fig.9. In all cases the arrivals of both the P and SV waves are observed. Their amplitudes are lowest for Model #1, followed by Model #2 -the peak amplitude of the signal corresponding to the P-wave is about 4 times bigger than that of Model #1- and highest for Model #3. In this case, the amplitude of the P-wave arrival is about three times larger than that of Model #2 and more than one order of magnitude larger than that of Model #1. The observed behavior is consistent with that observed in Fig.3, where the amplitude of both components of the electric field at the reservoir top followed the same amplitude pattern with respect to the three models; clearly this effect plays a role in the induced seismic interface responses. That is, the properties of all layers for the three models are the same, differing in just the geometry and number of horizontal conductive slabs. It is clear that more slabs yield stronger electromagnetic fields, and consequently, stronger z-components of the induced seismic interface response. However, as we have already mentioned, this trend is not monotonic. Because if the number of slabs is high

enough, the host layer becomes an homogeneous one, where no E_z can be created. Fig.10 depicts the recordings of the z component of the acceleration $\ddot{u}_z$ when Model #2 is considered. As it happened with the first model, the flat arrivals at about 0.15 s and 0.33 s associated with the P and SV waves generated at the reservoir top are clearly visible. The decay in amplitude at the center of the domain seems to be more pronounced for the SV-wave than in the previous case, while there is no remarkable change for the arrivals associated to the P-wave.

The surface recording for Model #3 does illustrate differences compared to the previous models, as can be seen in Fig.11, where we also show surface recordings of $\ddot{u}_z$. The arrivals of the seismic waves created at the reservoir top are neither flat, nor do they follow the same amplitude pattern as before. The variation in seismic amplitude has to do with the fact that the higher number of slabs located at different depths strongly impact the seismic wave created at the reservoir top. The superposition of the multiples results in waves recorded at different times at the surface. The arrivals at different times are both a consequence of the horizontal structure of the electric field at the reservoir top and the constructive and destructive superposition of the multiples. Another difference with the previous figures is the fact that the arrivals associated with the SV-wave have relatively weaker amplitudes with respect to the ones of the P-wave.

We display the energy densities of the three models in Fig.12 to quantitatively compare them. In the left panel of Fig.12, it can be seen that Model #3 generates the most energetic z-component response, followed by the one produced by Model #2, and finally, that of Model #1. The three energy densities present peaks at 0.15 s and 0.33 s, thus signaling the arrival times of the P-waves and SV-waves created at the reservoir top, respectively. It is remarkable that the P-wave peak of the Model #3 energy density is almost two (almost three) orders of magnitude higher than those of Model #2 (Model #1) respectively. The peaks associated with the SV-wave follow a similar trend, with the difference that the ones associated to Model #2 and Model #3 are closer to each other. The comparison of curves associated with x-component of the seismic signal is also interesting. They follow the same pattern as those of the orthogonal component; the one of Model #3 is the most energetic one, followed by those of Models #2 and #1 respectively. None of the responses shows a distinguishable peak associated to the SV-wave; however, as the number of slabs is increased, the peak associated to the arrival of the P-wave becomes more and more discernible. The P-wave response of Model #3 is about two orders of magnitude bigger than that of Model #2, and four orders of magnitude bigger than that of Model #1. The fact that the energy associated with this component increases with the number of slabs is a direct consequence of the increase of the amplitude of E_z at the reservoir top for the corresponding models.

5 OIL TRAPS IN A HYPOTHETICAL POP-UP STRUCTURE

We consider now a scenario, displayed in Fig.13, with a geometrical structure more elaborated than that of the previous models. In the considered situation, almost all components have the same physical properties as those of the same color in the previous models. The exception is the reservoir rock, which always contained oil (Layer #4 in Models #1, #2 and #3) but in the present case part of it is fully saturated with water (Reservoir rock, $S_w = 1$ in the figure). Its emerging properties are: $V_p = 2300$ m/s, $V_s = 1522$ m/s, $\sigma = 1.4 \times 10^{-3}$ S/m, $L_0 = 2.1 \times 10^{-10}$ A/(Pa m). We consider the primary electric field to have a time signature of a Ricker wavelet with 120 Hz central frequency and peak amplitude of 1 V/m. It is worth to mention here that the present scenario is less favorable for the conversions we are analyzing than that of Model #3; the slabs are replaced here by a unique conducting structure (the seal layer). This situation would be roughly comparable with a modification of Model #3, where only the set of slabs nearest to the reservoir top were considered. We have tested this model although we do not display the resulting fields, for the sake of brevity. We observed that the resulting electric field amplitudes are stronger than that of Models #1 and #2, but weaker than those of Model #3.

In Fig. 14 we display the spatial behaviour of the amplitudes of the electric field components E_x and E_z. They are, as before computed in the space-frequency domain, we take here the source peak frequency. The component E_x mostly follows the shape of the seal layer, and it does not clearly reveal to be affected by the presence of the oil reservoir. The presence of the oblique borders adjacent to the fractures induce charge accumulation there, yielding amplitudes for this component more than three times that of the incident plane wave, but not strongly enough to show the boundaries of the oil traps. The situation changes substantially when considering E_z. In this case, the discontinuity of the electric conductivity between the oil traps and their top and host layers produces strong jumps in the electric field, and the shape of the reservoirs can be plainly observed. We expect therefore that this situation will lead to recognizable hints of the presence of the oil traps in the corresponding component of the converted seismic signal.

Indeed, in the top left panel of Fig. 15 we display the traces registered on the surface of the z-component of the solid acceleration. Several diffraction points are visible, however, the overall response is not simple enough to undertake a straightforward interpretation. We therefore perform a depth Kirchhoff migration (Berkhout 1980) on this data, and obtain as a result the traces depicted in the top right panel. In this figure the three oil traps are clearly discernible. More importantly, not only their top boundaries are visible, but also their horizontal bottom limits are as well, which indicate the presence of the water-oil contact. This is consistent with what we mentioned in the Introduction, that in active source studies (Thompson et al. 2007; Hornbostel and Thompson 2007) the electroseismic conversions were detected at the boundary between the oil reservoir and the aquifer.

6 DISCUSSION

It is worth to mention that several scenarios were also considered besides the described ones. One of them was a variation of Model #3, where the subsurface was considered to be consolidated; that is, we assigned to layers 1 and 2 the same properties as layer 3. In this case, the peaks in the seismic energy density observed at the times associated with the arrival of the P and SV waves originated at the reservoir top were slightly lower -about 15%- than the one we display for this model in Fig.12. This is the expected behaviour of poorly consolidated (softer) layers allowing for a bigger amplitude of the seismic wave. Recall, however, that we consider rather low quality factors Q in the two low consolidated layers, to accurately take into account the velocity dispersion displayed by this kind of porous media.

Another considered scenario was to set layers 1 and 2 in model #3 with a partial water saturation $S_w = 0.4$, (see Tables 1 and 3). Naturally in this case, the vacant pore space was considered to be occupied by air. Due to this, the velocity of the seismic waves drops significantly in these layers, V_p is about 550 m/s. However, the height of the peaks of the seismic energy density was slightly lower than the original ones.

Yet another test was to consider a constant electrokinetic coupling coefficient throughout model #3. The reason behind this choice is that when performing field measurements it is quite complicated to get an estimate for an L_0 value for most formation components. This case also produced smaller seismic responses than the ones we display in the present work for the same model. A constant L_0 leaves the task of generating the electromagnetic to seismic conversions, for example at the reservoir top, to the contrasts in conductivity and mechanical properties between it and its overlying formation. Another point to take into account is that the depth migration of the seismic data performed in the last example assumes the prior knowledge of the seismic velocity structure of the subsurface. In a real scenario, this implies that the present study must be complemented with a purely seismic one, in order to this constraint to be fulfilled.

We are aware that the depth of the hydrocarbon reservoir we considered in our studies can't be considered a realistic one. However, we were interested in analyzing the existence of scenarios where normally incident plane waves, be their sources natural or man made, but upon which we have no control, can be strongly modified by laterally finite conductive channels, thus originating seismic responses at depth. Notice that for 2D slabs, the terminus is a line, or a rectangular area, for which the electric field spreading attenuation goes like distance to the inverse first power, assuming we are in the near-field limit where the target depth is smaller than the horizontal length of the dipole layer. For a rectangular electrode, the spreading attenuation is even smaller. Because of this, the analysis we present can be considered valid also for deeper reservoirs. Moreover, it is often assumed that the

skin depth places a limit on how deep an electromagnetic method will be useful. This is not really true. The depth limit depends on the sensitivity of the detection and the effort to collect data. At three skin depths, the signal is down by a factor of 20. That might not be a huge factor when sensitive methods and large efforts are employed. It is only when the depth is greater than about 3 skin depths that the exponential EM attenuation becomes unmanageable. We found that this observation can be important for the geometries we are dealing with and the expected overburden conductivity.

7 CONCLUSIONS

This work advances previous models of electroseismic conversion, with high-power active sources, by showing that also environmental electric fields might be useful in imaging the subsurface. We created different numerical models of various geometrical arrangements representing possible sets of plates created by natural random conductivity variations overlying a hydrocarbon reservoir. We have observed that thus created galvanic currents produce electric-field-to-seismic conversions at the top of the reservoir. The amplitudes of the converted seismic waves are different depending on the considered model and are highly sensitive to the oil content of the reservoir, the frequency of the primary electric field and the geometrical distribution of the conducting slabs.

For all models and frequencies, the electric fields at the reservoir are as large as or larger than the primary field. The amplitude and travel times of P and SV converted waves illustrate the possible usefulness of ES surveying for determining the depth of a target and a measure of its conductivity.

In particular, the amplitudes of the seismic energy densities were computed with different oil saturations. In each case the P-wave amplitude is substantially larger than the SV amplitude. The properties of the seismic response at the surface mimic the amplitudes of the electric fields at the reservoir. In addition to those features, the stack of conducting slabs in Model #3 create interference effects in the seismic waves. The Model #3 amplitudes are substantially larger than Models #1 and #2, partially because the lowest conducting slabs are near the reservoir. The existence of interference among the slabs is seen in the distribution of arrival times at the surface.

The employed source amplitude is compatible with measured natural electric fields (Nicoll et al. 2019) and the computed amplitudes of the seismic waves are in the order of measurable accelerations. However, other studies have pointed out that there are many geometrical and material properties that can alter the electroseismic response by orders of magnitude. Thin layering, the impact of the Biot slow waves, and other factors can influence the amplitudes by large amounts. Those analyses are for future studies.

ACKNOWLEDGEMENTS

F.Z. acknowledges support from CONICET through grant PIP 112-201501-00192. L.J., L.M. and F.Z. acknowledge support from CNRS/INSU through the PICS SEISMOFLUID. The numerical simulations were performed in TUPAC, the CSC-CONICET computing cluster; special thanks to the system administrators D. Vinazza and E. Mocksos for their helpfulness. L.M. acknowledges Dr. Jorge Albano for being his first mentor on the study of the electrokinetic phenomena. All data produced in this work are available and can be requested to the e-mail zyserman@fcaglp.unlp.edu.ar

REFERENCES

Allègre, V., Jouniaux, L., Lehmann, F., Sailhac, P., 2010. Streaming Potential dependence on water-content in fontainebleau sand. Geophys. J. Int. 182, 1248–1266. doi:10.1111/j.1365-246X.2010.04716.x.

Allègre, V., Jouniaux, L., Lehmann, F., Sailhac, P., Toussaint, R., 2015. Influence of water pressure dynamics and fluid flow on the streaming-potential response for unsaturated conditions. Geophysical Prospecting 63, 694–712. doi:10.1111/1365-2478.12206.

Allègre, V., Lehmann, F., Ackerer, P., Jouniaux, L., Sailhac, P., 2012. Modelling the streaming potential dependence on water content during drainage: 1. A 1D modelling of SP using finite element method. Geophys. J. Int. 189, 285–295. doi:10.1111/j.1365-246X.2012.05371.x.

Allegre, V., Maineult, A., Lehmann, F., Lopes, F., Zamora, M., 2014. Self-potential response to drainage-imbibition cycles. Geophys. J. Int. 197, 1410–1424. doi:10.1093/gji/ggu055.

Berkhout, A., 1980. Seismic Migration, Imaging of Acoustic Energy by Wave Field Extrapolation. Elsevier.

Bordes, C., Sénéchal, P., Barrière, J., Brito, D., Normandin, E., Jougnot, D., 2015. Impact of water saturation on seismoelectric transfer functions: a laboratory study of coseismic phenomenon. Geophys. J. Int. 200, 1317–1335.

Brovelli, A., Cassiani, G., Dalla, E., Bergamini, F., Pitea, D., Binley, A.M., 2005. Electrical properties of partially saturated sandstones: Novel computational approach with hydrogeophysical applications. Water Resources Research 41, 12pp.

Butler, K.E., Kulessa, B., Pugin, A.J., 2018. Multimode seismoelectric phenomena generated using explosive and vibroseis sources. Geophysical Journal International 213, 836–850.

Carcione, J., Picotti, S., 2006. P-wave seismic attenuation by slow-wave diffusion: effects of inhomogeneous rock properties. Geophysics 71, O1–O8.

Carcione, J., Seriani, G., Gei, D., 2003. Acoustic and electromagnetic properties of soil saturated with salt water and NAPL. J. Appl. Geophys. 52, 177–191.

Castromán, G., Rubino, G., Barbosa, N., Zyserman, F., Holliger, K., 2020. Fluid pressure diffusion effects on the excess compliance matrix of porous rocks containing aligned fractures. Geophys. J. Int. 222, 715–733.

Chotiros, N., Isakson, M., 2004. A broadband model of sandy ocean sediments: Biot-Stoll with contact squirt flow and shear drag. J. Acoust. Soc. Am. 116, 2011–2022.

Corredor, R.M., Santos, J., Gauzellino, P., Carcione, J., 2014. Reflection and transmission coefficients of a single layer in poroelastic media. J. Acoust. Soc. Am. 135, 3151–3162.

Devi, M., Garambois, S., , Brito, D., Dietrich, M., Poydenot, V., Bordes, C., 2018. A novel approach for seismoelectric measurements using multielectrode arrangements-II: laboratory measurements. Geophys. J. Int. 214, 1783–1799. doi:10.1093/gji/ggy251.

Dietrich, M., Devi, M., Garambois, S., , Brito, D., Bordes, C., 2018. A novel approach for seismoelectric measurements using multielectrode arrangements-I: theory and numerical experiments. Geophys. J. Int. 215, 61–80. doi:10.1093/gji/ggy269.

Dupuy, B., Garambois, S., Virieux, J., 2016. Estimation of rock physics properties from seismic attributes - Part 1: Strategy and sensitivity analysis. Geophysics 80, M35–M53. doi:10.1190/GEO2015-0239.1.

Dzieran, L., Thorwart, M., Rabbel, W., 2020. Seismoelectric monitoring of aquifers using local seismicity-a feasibility study. Geophysical Journal International 222, 874–892. doi:10.1093/gji/ggaa206.

Dzieran, L., Thorwart, M., Rabbel, W., Ritter, O., 2019. Quantifying interface responses with seismoelectric spectral ratios. Geophysical Journal International 217, 108–121.

Fiorentino, E., Toussaint, R., Jouniaux, L., 2017. Two-phase lattice boltzmann modelling of streaming potentials: influence of the gas-water interface on the electrokinetic coupling. Geophys. J. Int. 208, 1139–1156. doi:https://doi.org/10.1093/gji/ggw417.

Gao, Y., Wang, D., Yao, C., , Guan, W., Hu, H., Zhang, W., Tong, P., Yang, Q., 2019. Simulation of seismoelectric waves using finite-difference frequency-domain method: 2D SHTE mode. Geophys. J. Int. 216, 414–438. doi:10.1019/gji/ggy443.

Garambois, S., Senechal, P., Perroud, H., 2002. On the use of combined geophysical methods to access water content and water conductivity of near surface formations. J. Hydrol. 259, 32–48.

Gauzellino, P., Carcione, J., Santos, J., Picotti, S., 2014. A rheological equation for an isotropic-anelastic media and simulation of field seismograms. Wave motion 51, 743–757.

Gershenzon, N.I., Bambakidis, G., Ternovskiy, I., 2014. Coseismic electromagnetic field due to the electrokinetic effect. Geophysics 79(5), E217–E229.

Glover, P., Peng, R., Lorinczi, P., Di, B., 2019. Experimental measurement of frequency-dependent permeability and streaming potential of sandstones. Transport in Porous Media 131, 333–361. doi:10.1007/s11242-019-01344-5.

Grobbe, N., Revil, A., Zhu, Z., Slob, E. (Eds.), 2020. Seismoelectric Exploration: Theory, Experiments, and Applications. Geophysical Monograph Series, Wiley.

Haartsen, M.W., Pride, S., 1997. Electroseismic waves from point sources in layered media. J. Geophys. Res. 102, 24,745–24,769.

Haines, S.H., Pride, S.R., 2006. Seismoelectric numerical modeling on a grid. Geophysics 71, 57–65.

Hornbostel, S., Thompson, A., 2007. Waveform design for electroseismic exploration. Geophysics 72, Q1–Q10. doi:10.1190/1.2436473.

Jaafar, M.Z., Vinogradov, J., Jackson, M.D., 2009. Measurement of streaming potential coupling co-

efficient in sandstones saturated with high salinity nacl brine. Geophys. Res. Lett. 36, L21306. doi:10.1029/2009GL040549.

Jougnot, D., Linde, N., Haarder, E., Looms, M., 2015. Monitoring of saline tracer movement with vertically distributed self-potential measurements at the HOBE agricultural site, Voulund, Denmark. Journal of Hydrology 521, 314–327. doi:10.1016/j.jhydrol.2014.11.041.

Jougnot, D., Linde, N., Revil, A., Doussan, C., 2012. Derivation of soil-specific streaming potential electrical parameters from hydrodynamic characteristics of partially saturated soils. Vadose Zone J. 11. doi:10.2136/vzj2011.0086.

Jougnot, D., Roubinet, D., Guarracino, L., Maineult, A., 2020. Modeling streaming potential in porous and fractured media, description and benefits of the effective charge density approach, in: Biswas, A., Sharma, A. (Eds.), Advances in Modeling and Interpretation in Near Surface Geophysics. Springer. Springer Geophysics. chapter 4, pp. 61–96.

Jouniaux, L., Ishido, T., 2012. Electrokinetics in Earth Sciences: a tutorial. Int. J. Geophysics vol. 2012, Article ID 286107. doi:10.1155/2012/286107.

Jouniaux, L., Zyserman, F., 2016. A review on electrokinetically induced seismo-electrics, electro-seismics, and seismo-magnetics for Earth sciences. Solid Earth 7, 249–284. doi:10.5194/se-7-249-2016.

Liu, H.P., Don, L., Kanamori, H., 1976. Velocity dispersion due to anelasticity; implications for seismology and mantle composition. J. Geophys. Res. , 41–58.

Løseth, L., Pedersen, H., Ursin, B., Amundsen, L., Ellingsrud, S., 2006. Low-frequency electromagnetic fields in applied geophysics: Waves or diffusion? Geophysics 71, W29–W40.

Manassero, M., Afonso, J., Zyserman, F., Zlotnik, C., Fomin, I., 2020. A reduced order approach for probabilistic inversions of 3D magnetotelluric data I: General formulation. Geophysical Journal International 223, 1837–1863.

Martner, S.T., Sparks, N.R., 1959. The electroseismic effect. Geophysics 24, 297–308.

Mavko, G., Mukerji, T., Dvorkin, J., 2009. The rock physics handbook: Tools for seismic analysis of porous media. Cambridge University Press, The Pitt Building, Trumpington Street, Cambridge CB2 IRP, United Kingdom.

Monachesi, L., Zyserman, F., Jouniaux, L., 2018a. An analytical solution to assess the SH seismoelectric response of the vadose zone. Geophys. J. Int. 213, 1999–2019.

Monachesi, L., Zyserman, F., Jouniaux, L., 2018b. SH Seismoelectric Response of a Glacier: An Analytic Study. J. Geophys. Res.: Earth Surface 123, 2135–2156. doi:10.1029/2018JF004607.

Munch, F., Zyserman, F., 2016. Detection of Non-Aqueous Phase Liquids Contamination by SH-TE Seismoelectrics: a Computational Feasibility Study. Journal of Applied Geophysics doi:10.1016/j.jappgeo.2016.03.026.

Nicoll, K., Harrison, R., Barta, V., Bor, J., Brugge, R., Chillingarian, A., Chum, J., Georgoulias, A., Guha, A., Kourtidis, K., Kubicki, M., Mareev, E., Matthews, J., Mkrtchyan, H., Odzimek, A., Raulin, J.P., Robert, D., Silva, H., Tacza, J., Yair, Y., Yaniv, R., 2019. A global atmospheric electricity monitoring network

for climate and geophysical research. Journal of Atmospheric and Solar-Terrestrial Physics 184, 18–29. doi:https://doi.org/10.1016/j.jastp.2019.01.003.

Peng, R., Di, B., Glover, P.W.J., Wei, J., Lorinczi, P., Liu, Z., Li, H., 2020. Seismo-electric conversion in shale: experiment and analytical modelling. Geophysical Journal International 223, 725–745. doi:10.1093/gji/ggaa288.

Peng, R., Di, B., Wei, J., Ding, P., Zhao, J., Pan, X., Liu, Z., 2017. Experimental study of the seismoelectric interface response in wedge and cavity models. Geophys. J. Int. 210, 1703–1720. doi:10.1093/gji/ggx253.

Perrier, F., Morat, P., 2000. Characterization of electrical daily variations induced by capillary flow in the non-saturated zone. Pure Appl. Geophys. 157, 785–810.

Pride, S., 1994. Governing equations for the coupled electromagnetics and acoustics of porous media. Phys. Rev. B 50, 15678–15695.

Pride, S., Morgan, F.D., 1991. Electrokinetic dissipation induced by seismic waves. Geophysics 56, 914–925.

Pride, S.R., 2005. Relationships between seismic and hydrological properties, in: Rubin, Y., Hubbard, S. (Eds.), Hydrogeophysics. Springer. chapter 9, pp. 253–290.

Raab, F.H., 2010. Noise model for low-frequency through-the-earth communication. Radio Sci. 45, RS6019, RS6019. doi:10.1029/2010RS004378.

Rakov, V., Uman, M., 2003. Frontmatter. In Lightning: Physics and Effects (pp. I-VI). Cambridge: Cambridge University Press.

Ren, H., Huang, Q., Chen, X., 2016. Existence of evancescent electromagnetic waves resulting from seismo-electric conversion at a solid-porous interface. Geophys. J. Int. 204, 147–166. doi:10.1093/gji/ggv400.

Ren, H., Huang, Q., Chen, X., 2018. Quantitative understanding on the amplitude decay characteristic of the evanescent electromagnetic waves generated by seismoelectric conversion. Pure and Applied Geophysics 175, 2853–2879.

Rosas-Carbajal, M., Jougnot, D., Rubino, J., Monachesi, L., Linde, N., Holliger, K., 2020. Seismoelectric Signals Producedc by Mesoscopic Heterogeneities, in: Grobbe, N., Revil, A., Zhu, Z., Slob, E. (Eds.), Seismoelectric Exploration: Theory, Experiments, and Applications. Wiley. chapter 19, pp. 249–287.

Santos, J., Ravazzoli, C., Gauzellino, P., Carcione, J., 2005. Numerical simulation of ultrasonic waves in reservoir rocks with patchy saturation and fractal petrophysicas properties. Computational Geosciences 9, 1–27.

Santos, J., Ravazzoli, C., Gauzellino, P., Carcione, J., Cavallini, F., 2004. Simulation of waves in poro-viscoelastic rocks saturated by immiscible fluids. numerical evidence of a second slow wave. J. Comput. Acoust. 12, 1–21.

Santos, J., Zyserman, F., Gauzellino, P., 2012. Numerical electroseismic modeling: A finite element approach. Applied Mathematics and Computation 218, 6351–6374.

Schön, J., 1996. Physical properties of rocks - fundamentals and principles of petrophysics. volume 18. Elsevier Science Ltd., Handbook of Geophysical Exploration, Seismic exploration.

Simpson, F., Bahr, K., 2005. Practical magnetotellurics. Cambridge University Press.

Smeulders, D.M.J., Grobbe, N., Heller, H.K.J., Schakel, M., 2014. Seismoelectric conversion for the detection of porous medium interfaces between wetting and nonwetting fluids. Vadose Zone J. doi:10.2136/vzj2013.06.0106.

Strahser, M., Jouniaux, L., Sailhac, P., Matthey, P.D., Zillmer, M., 2011. Dependence of seismoelectric amplitudes on water-content. Geophys. J. Int. 187, 1378–1392.

Teja, A.S., Rice, P., 1981. Generalized corresponding states method for the viscosities of liquid mixtures. Ind. Eng. Chem. Fund. 20, 77–81.

Thompson, A., Hornbostel, S., Burns, J., Murray, T., Raschke, R., Wride, J., McCammon, P., Bixby, M., Ross, W., White, B., Zhou, M., 2007. Field tests of electroseismic hydrocarbon detection. Geophysics 72, N1–N9.

Thompson, A.H., Gist, G.A., 1993. Geophysical applications of electrokinetic conversion. The Leading Edge 12, 1169–1173.

Thompson, R.R., 1936. The seismic-electric effect. Geophysics 1, 327–335.

Wang, D., Gao, Y., Yao, C., Wang, B., Wang, M., 2020a. Seismoelectric and electroseismic responses to a point source in a marine stratified model. Geophysical Prospecting 68, 1958–1979. doi:10.1111/1365-2478.12948.

Wang, J., Zhu, Z., Gao, Y., Morgan, F.D., Hu, H., 2020b. Measurements of the seismoelectric responses in a synthetic porous rock. Geophysical Journal International 222, 436–448. doi:10.1093/gji/ggaa174.

Wang, J., Zhu, Z., Guan, W., Gao, Y., Wu, X., 2021. Experimental studies on the mechanism of seismoelectric logging while drilling with multipole source. Geophysical Journal International 225, 445–455.

Wang, W., Cui, Z., Liu, J., Kundu, T., 2020c. Dependence of borehole shear-horizontal-wave seismoelectric response on soil textures. Geophysical Prospecting 69, 250–266.

Ward, S., Hohmann, G.W., 1987. Electromagnetic theory for geophysical applications, in: Nabiguian, M.N. (Ed.), Electromagnetic Methods in Applied Geophysics. SEG. volume 1 of *SEG Investigations in Geophysics 3*.

Warden, S., Garambois, S., Jouniaux, L., Brito, D., Sailhac, P., Bordes, C., 2013. Seismoelectric wave propagation numerical modeling in partially saturated materials. Geophys. J. Int. 194, 1498–1513. doi:10.1093/gji/ggt198.

White, B., Zhou, M., 2006. Electroseismic prospecting in layered media. SIAM J. on Applied Mathematics 67, 69–98.

Zhdanov, M., 2009. Geophysical Electromagnetic Theory and Methods. Elsevier.

Zhu, Z., Toksöz, M., Burns, D., 2008. Electroseismic and seismoelectric measurements of rock sample in a water tank. Geophysics 73, E153–E164. doi:10.1190/1.2952570.

Zyserman, F., Gauzellino, P., Jouniaux, L., 2020. Finite Element Modeling of Electroseismics and Seismoelectrics, in: Grobbe, N., Revil, A., Zhu, Z., Slob, E. (Eds.), Seismoelectric Exploration: Theory, Experiments, and Applications. Wiley. chapter 18, pp. 245–267.

Zyserman, F., Gauzellino, P., Santos, J., 2010. Finite element modeling of SHTE and PSVTM electroseismics. J. Applied Geophysics 72, 79–91. doi:10.1016/j.jappgeo.2010.07.004.

Zyserman, F., Gauzellino, P., Santos, J., 2012. Numerical evidence of gas hydrate detection by means of

electroseismics. J. Applied Geophysics 86, 98–108.

Zyserman, F., Jouniaux, L., Warden, S., Garambois, S., 2015. Borehole seismoelectric logging using a shear-wave source:Possible application to CO_2 disposal? International Journal of Greenhouse Gas Control 33, 82–102. doi:10.1016/j.ijggc.2014.12.009.

Zyserman, F., Monachesi, L., Jouniaux, L., 2017a. Dependence of shear wave seismoelectrics on soil textures: a numerical study in the vadose zone. Geophys. J. Int. 208, 918–935.

Zyserman, F., Monachesi, L., Jouniaux, L., 2017b. Reply to "Comment on "Dependence of shear wave seismoelectrics on soil textures: a numerical study in the vadose zone by F.I. Zyserman, L.B. Monachesi and L. Jouniaux" by Revil, A. Geophys. J. Int. 210, 1652–1658.

Zyserman, F., Santos, J., 2007. Analysis of the numerical dispersion of waves in saturated poroelastic media. Comput. Methods Appl. Mech. Engrg. 196, 4644–4655.

Basic parameters I					
Parameter	Layer 1	Layer 2	Layer 3	Layer 4	Slabs
ϕ [-]	0.41	0.41	0.15	0.25	0.20
β_{sand} [-]	0.95	0.95	1.0	1.0	0.90
β_{clay} [-]	0.05	0.05	0.0	0.0	0.10
$Q_{p,s}$ [-]	40	45	500	500	500
C_0 [mol/l]	2.0×10^{-3}	2.0×10^{-3}	2.0×10^{-3}	1.0×10^{-5}	5.0×10^{-1}
S_w [-]	1 (0.6)	1 (0.6)	1	$^{(A)}$ 0.85 $^{(B)}$ 0.60 $^{(C)}$ 0.10	1

Table 1. Basic parameters characterizing each structure in all considered subsurface models. Values between brackets for the water saturation in layers #1 and #2 correspond to the partial saturation case addressed in the Discussion section.

Basic parameters II	
$\hat{m}$	1.85
$\hat{n}$	2.05
$K_{s,\text{sand}}$ [GPa]	36
$K_{s,\text{clay}}$ [GPa]	20.9
$G_{s,\text{sand}}$ [GPa]	45
$G_{s,\text{clay}}$ [GPa]	6.8
$\rho_{s,sand}$ [kg/m^3]	2600
$\rho_{s,clay}$ [kg/m^3]	2580
$r_{s,sand}$ [m]	8.0×10^{-5}
$r_{s,clay}$ [m]	5.0×10^{-7}
C_s [-]	10
K_w [GPa]	2.25
η_w [Pa.s]	1.0×10^{-3}
ρ_w [kg/m^3]	1.0×10^3
ϵ_w [F/m]	80 ϵ_0
K_{oil}[GPa]	0.8
η_{oil} [Pa.s]	2.5×10^{-2}
ρ_{oil} [kg/m^3]	0.88×10^3
K_{air}[GPa]	1.4×10^{-4}
η_{air} [Pa.s]	1.8×10^{-5}
ρ_{air} [kg/m^3]	1.23
T [K]	298

Table 2. Basic parameters common to all models

Parameter	Layer 1	Layer 2	Layer 3	Layer 4	Slabs
σ [S/m]	3.7×10^{-3} (1.4×10^{-3})	3.7×10^{-3} (1.4×10^{-3})	5.6×10^{-4}	$^{(A)}8.5 \times 10^{-6}$ $^{(B)}5.3 \times 10^{-6}$ $^{(C)}2.5 \times 10^{-6}$	0.23
L_0 [A/(Pa m)]	1.4×10^{-9} (6.5×10^{-9})	1.4×10^{-9} (6.5×10^{-9})	2.9×10^{-11}	$^{(A)}4.0 \times 10^{-10}$ $^{(B)}3.7 \times 10^{-9}$ $^{(C)}1.2 \times 10^{-10}$	2.87×10^{-11}
V_p [m/s]	1678 (560)	1678 (560)	3757	$^{(A)}2745$ $^{(B)}2643$ $^{(C)}2557$	3091
V_s [m/s]	301 (323)	301 (323)	2233	$^{(A)}1523$ $^{(B)}1526$ $^{(C)}1530$	1590

Table 3. Subsurface properties, obtained using the rock physics models displayed in Section 2.1 and basic parameters from Table 2 and Table 1. Walton's model does not create appreciable differences in velocities between Layer 1 and Layer 2, but the latter is set more anelastic than the former. The electric conductivity, electrokinetic coupling coefficient and seismic velocities in Layer 4 correspond to an oil saturation of (A) 15%, (B) 40%, (C) 90%. Values between brackets for the electric conductivity, electrokinetic coupling coefficient and seismic velocities in layers #1 and #2 correspond to the partial saturation case addressed in the Discussion section.

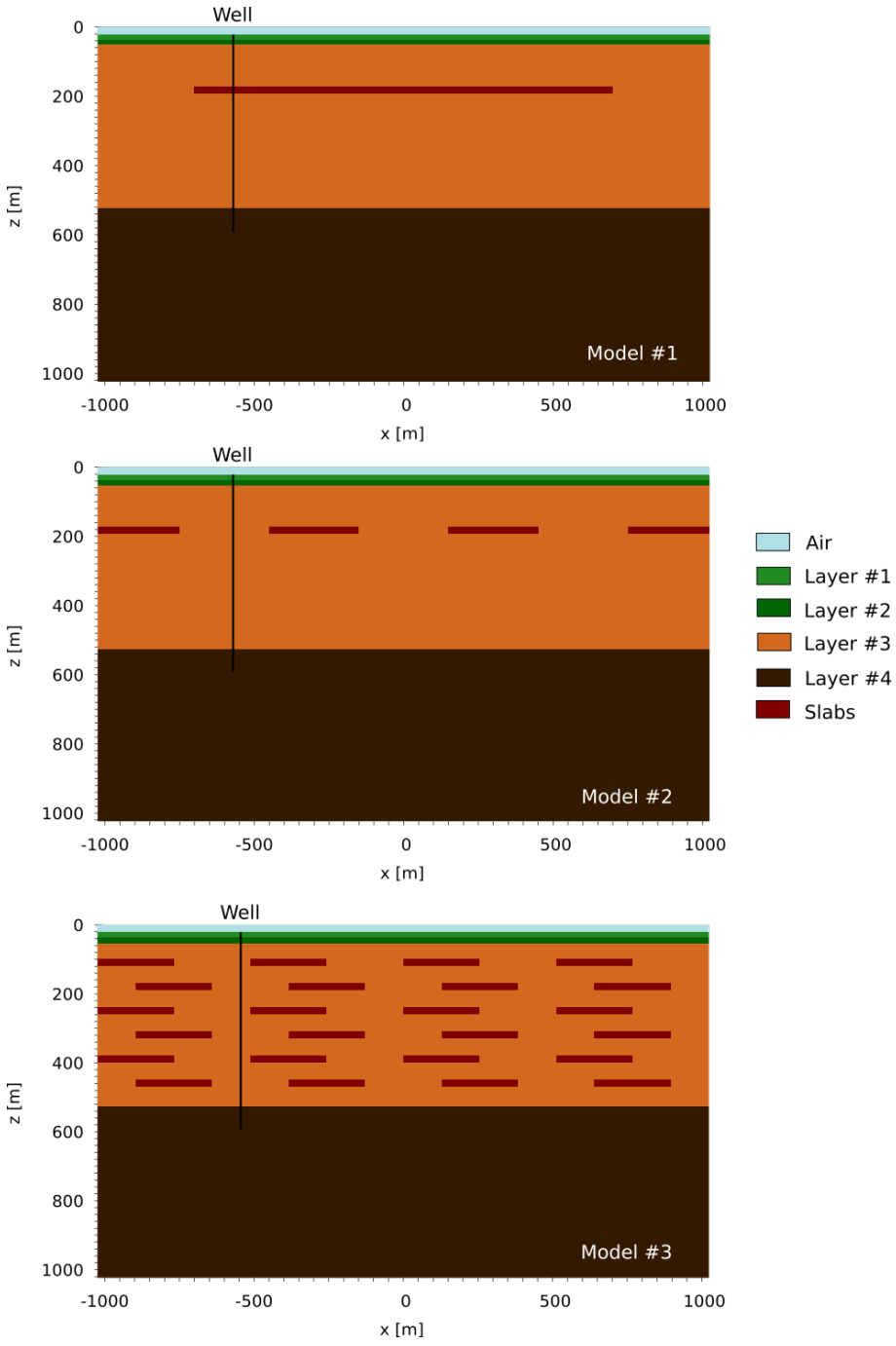

Figure 1. Scaled representation of the first three models analyzed in this work. One hundred receivers, from -800 m to 800 m separated 16 m from each other are located on the Earth's surface along the x-direction. In the well, starting at the surface, the same number of receivers is set, separated 6 m from each other. Material properties are described in Table 1.

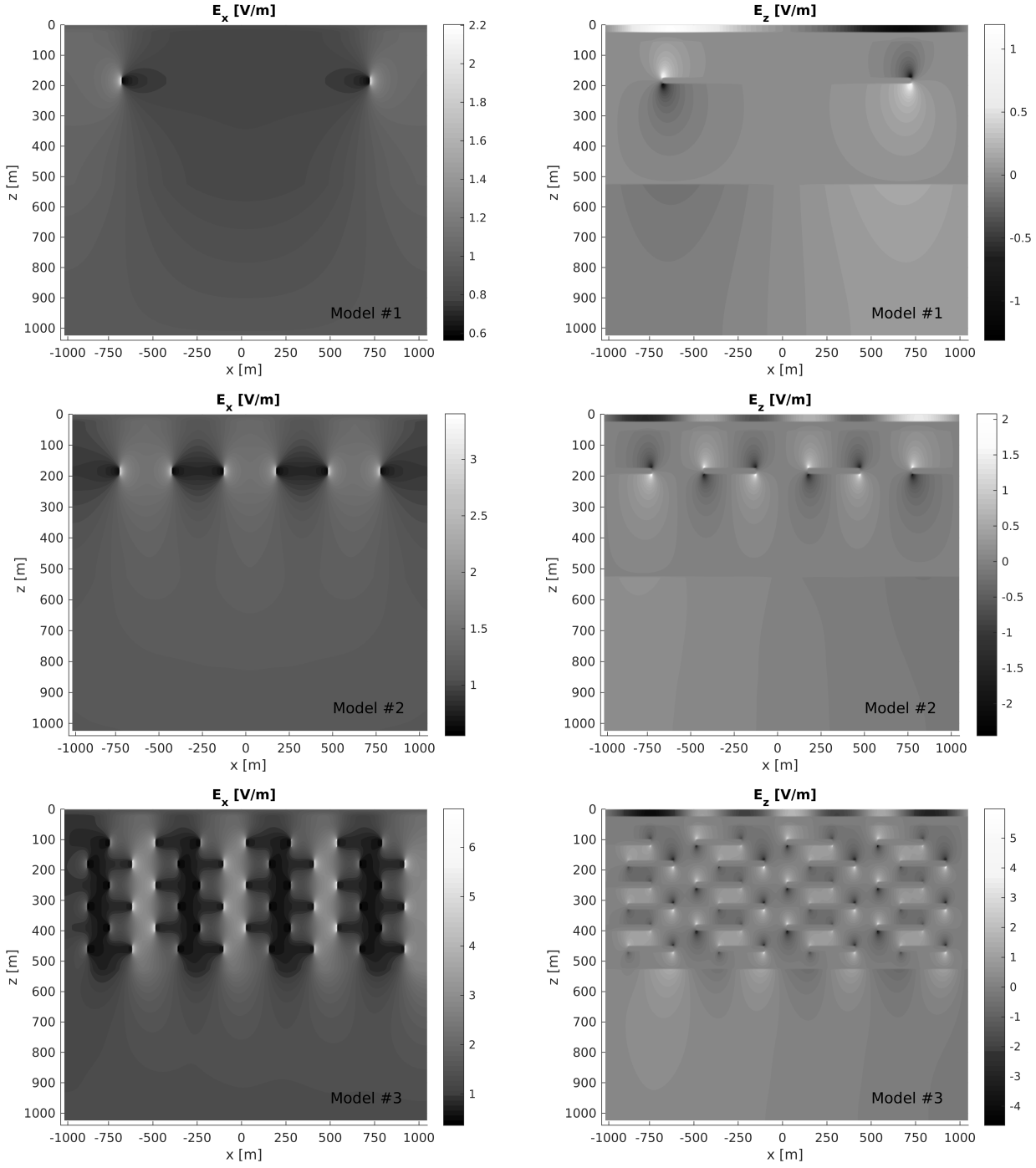

Figure 2. Magnetotelluric electric field, computed in the frequency domain, at a sigle frequency $f = 0.01$ Hz. The origin of the z-axis is located at the Earth's surface, meanwhile the corresponding origin for the x-axis is located at the middle point of the whole structure

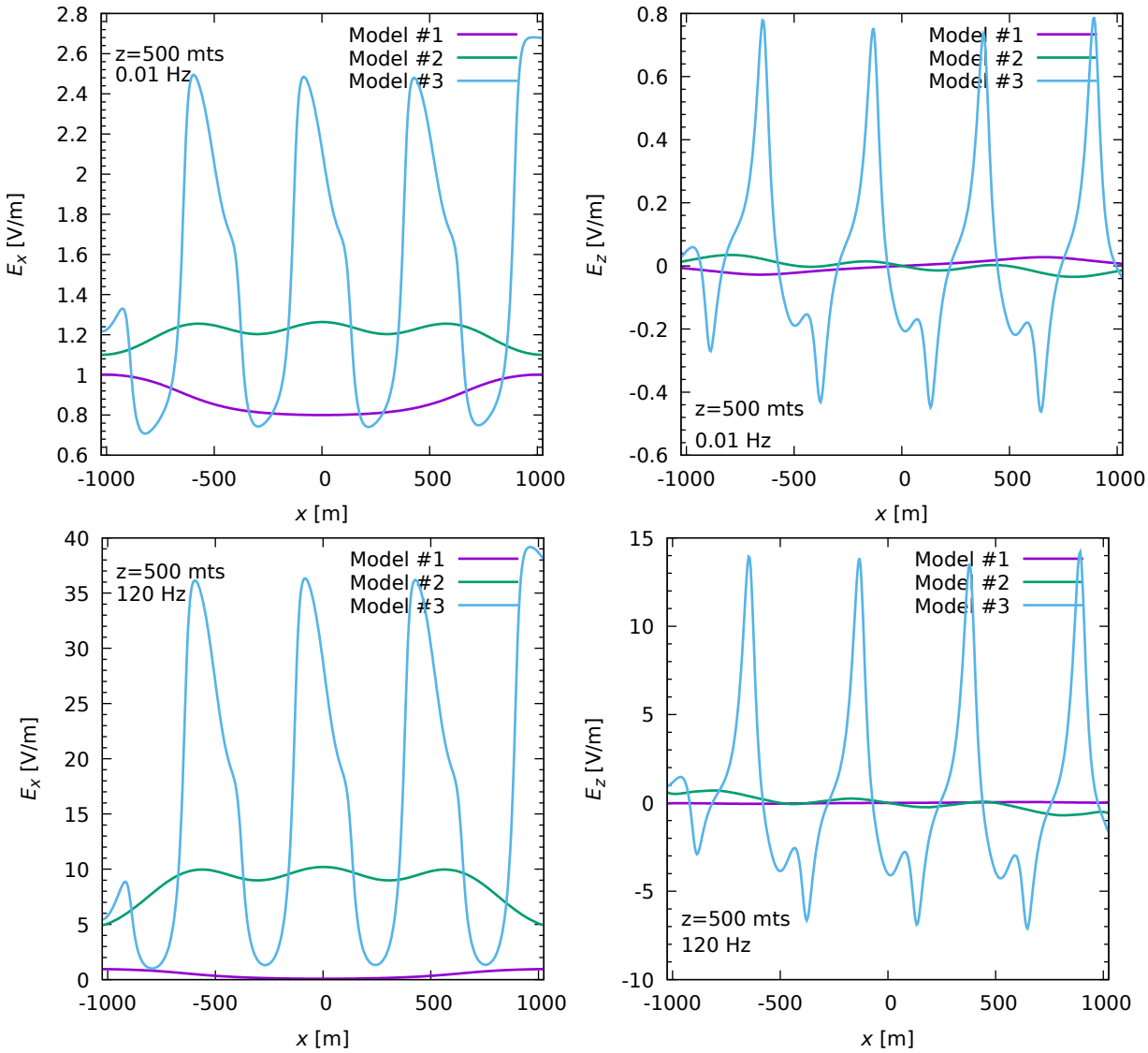

Figure 3. Comparison of the amplitude of the electric fields displayed in the previous figure, for the three models, at the reservoir top. Top panels correspond to a frequency of 0.01 Hz meanwhile the bottom panels to 120 Hz.

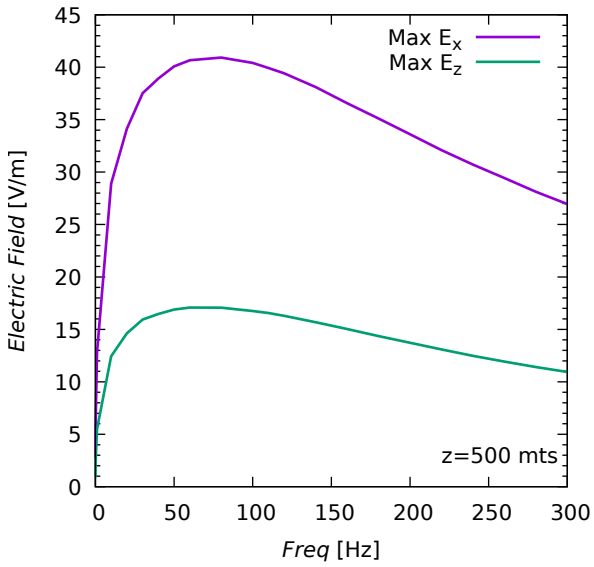

Figure 4. Electric field amplitude maxima for Model #3 as a function of frequency, both components, considered at $z = 500$ m depth.

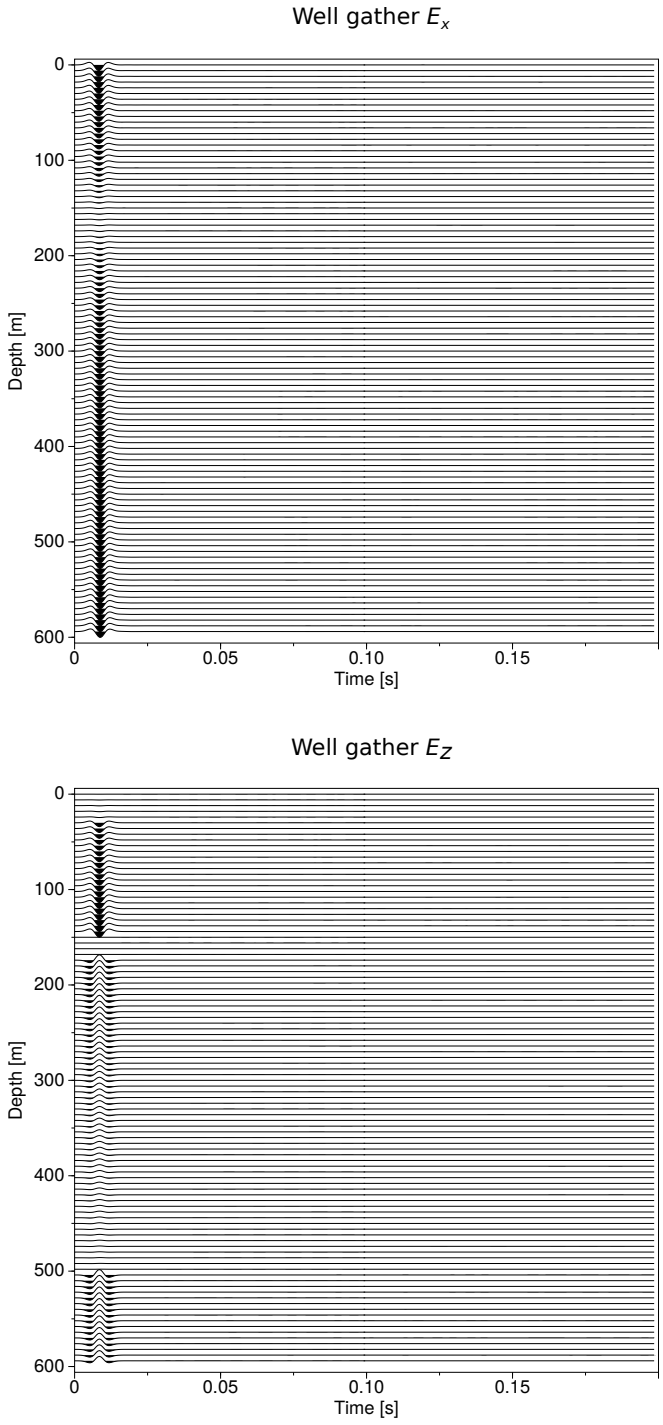

Figure 5. Well gathers of the magnetotelluric electric field components, considering Model #1.

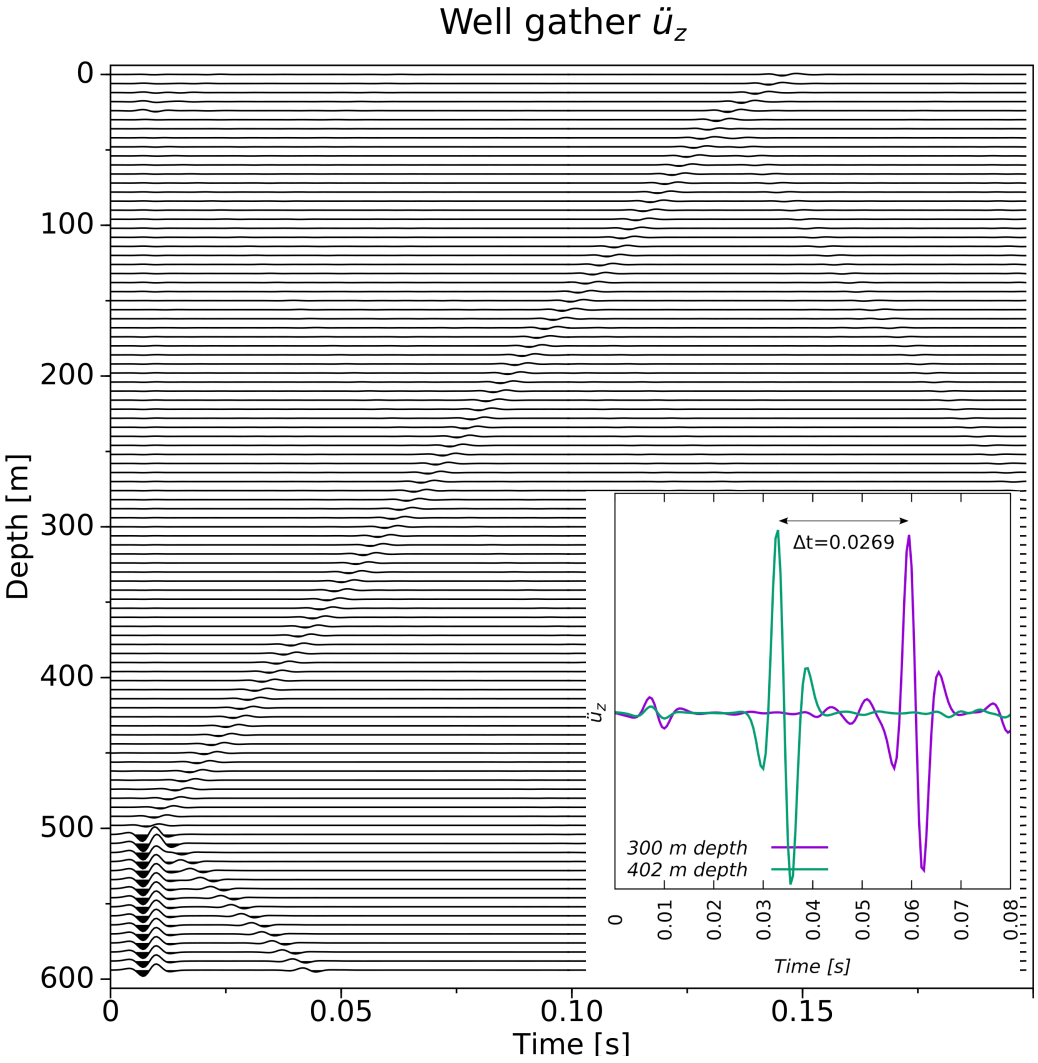

Figure 6. Well gather of the vertical component of the seismic wave acceleration $\ddot{u}_z$, considering Model #1. The upwards traveling wave originated at 500 mts depth hits the surface at about 0.15 s

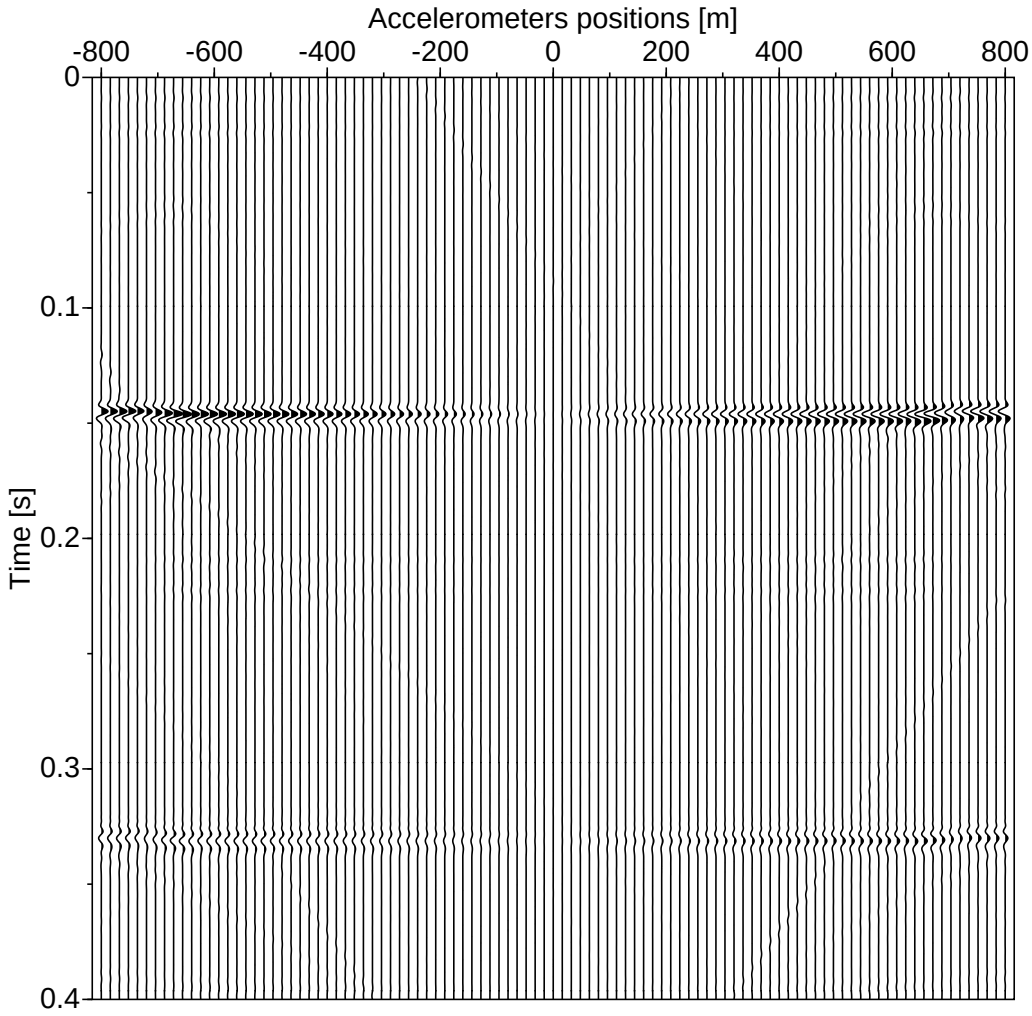

Figure 7. Gather of the vertical component of the seismic wave acceleration $\ddot{u}_z$, recorded at the surface, considering Model #1. The upwards traveling waves originated at 500 mts depth hit the surface at about 0.15 s, at a time compatible with the P-wave velocity, and at about 0.33 s, at a time compatible with the SV-wave velocity.

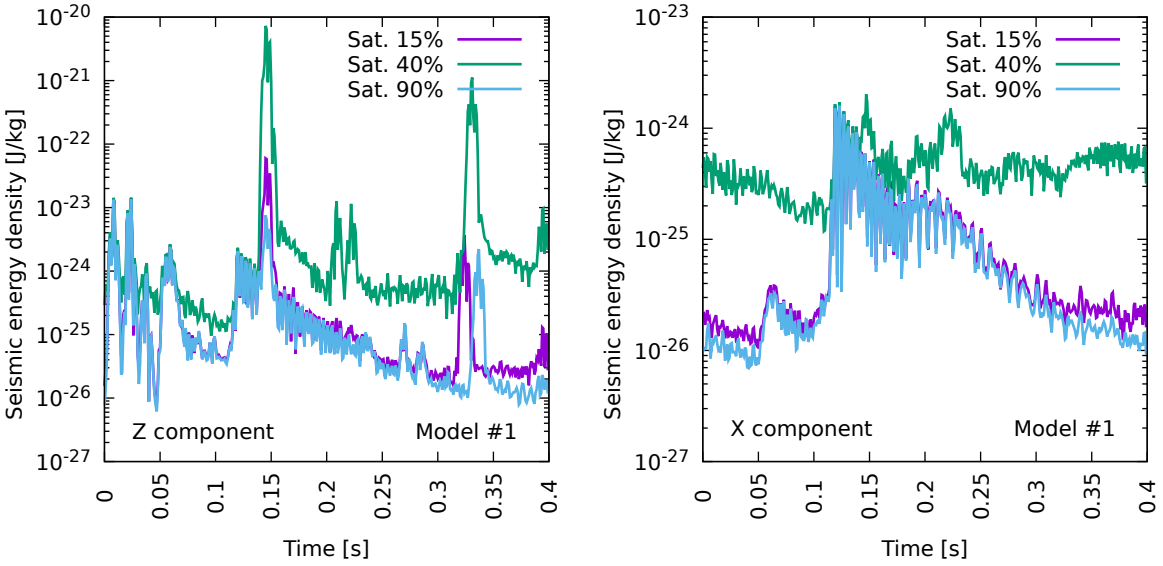

Figure 8. Comparison the seismic energy density for different oil saturations in the reservoir, considering Model #1. The curves are obtained by stacking the squared traces for $\dot{u}_z$ (left panel) and $\dot{u}_x$ (right panel) recorded in all surface receivers, and dividing by the number of receivers.

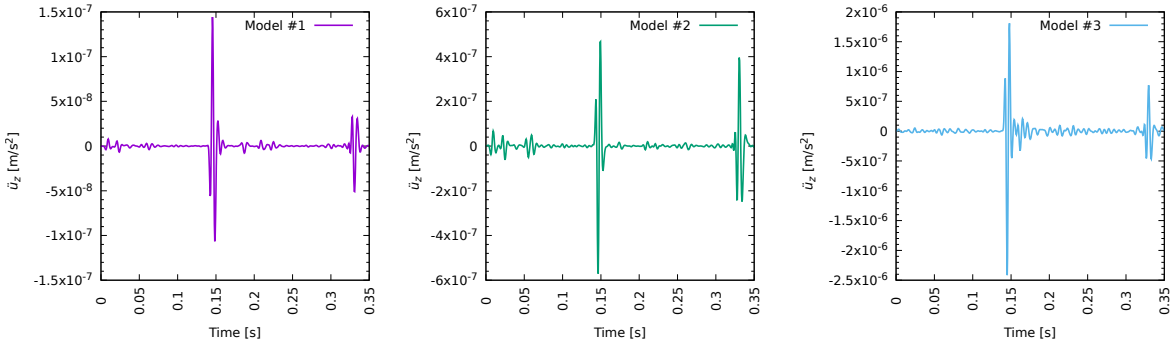

Figure 9. Acceleration traces recorded on the surface (z component), at the well position, considering Model #1, Model #2 and Model #3. In all cases a 40% oil saturation in the reservoir was considred.

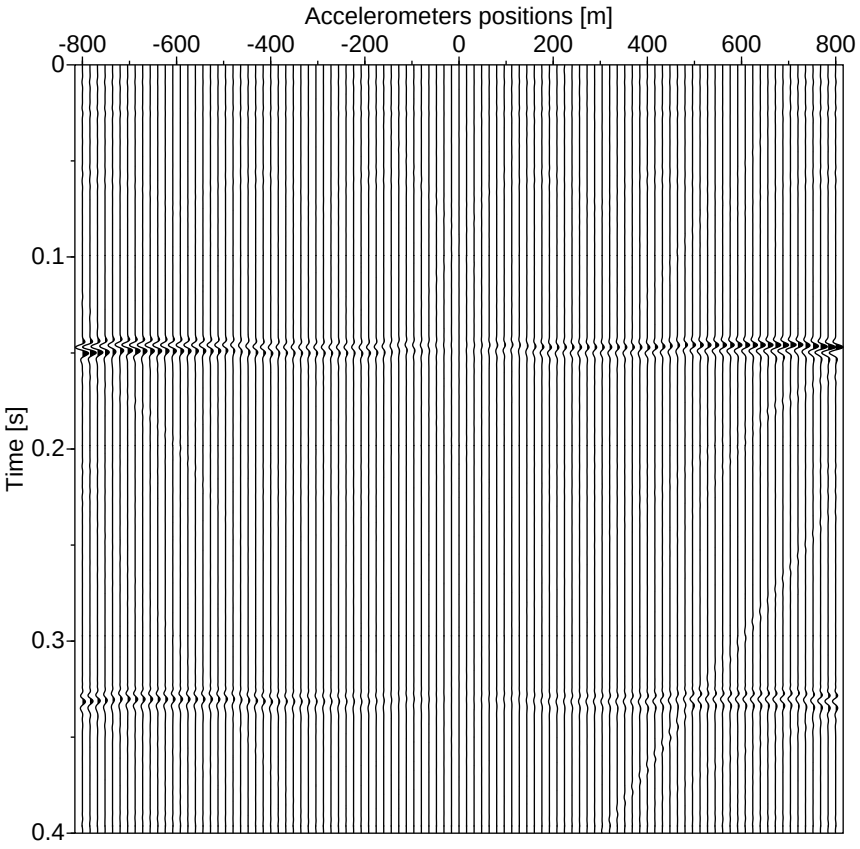

Figure 10. Gather of the vertical component of the seismic wave acceleration $\ddot{u}_z$, recorded at the surface, considering Model #2. The upwards traveling waves originated at 500 mts depth hit the surface at about 0.15 s, at a time compatible with the P-wave, and at about 0.33 s, at a time compatible with the SV-wave.

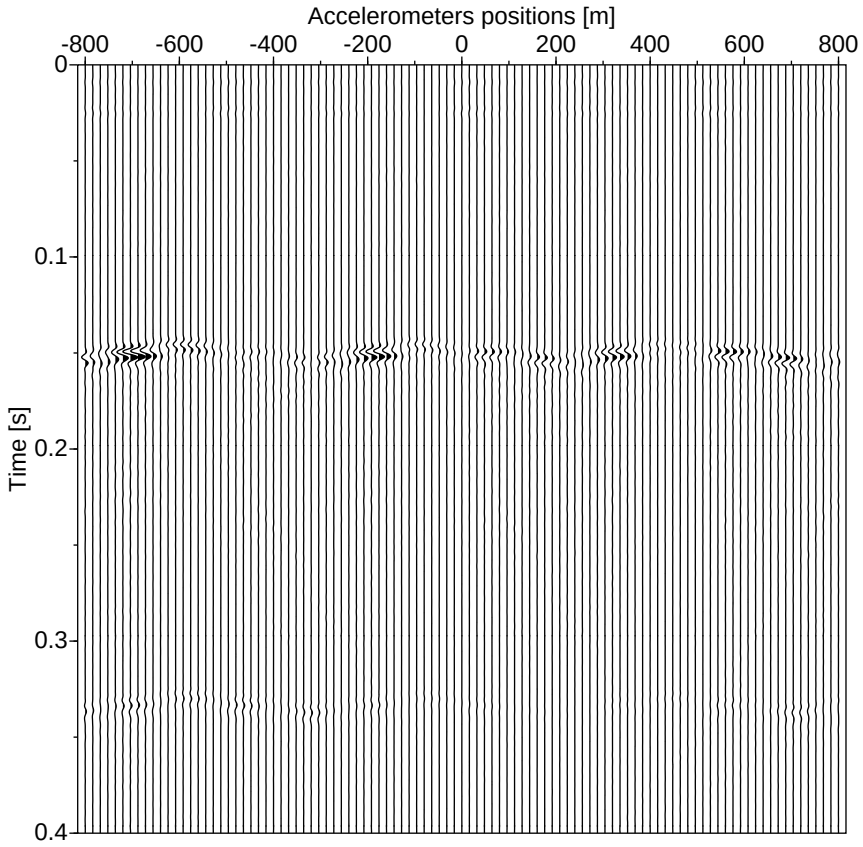

Figure 11. Gather of the vertical component of the seismic wave acceleration $\ddot{u}_z$, recorded at the surface, considering Model #3. Although the wavefronts originated at the reservoir top are clearly discernible, they are weaker than the ones in Fig.10, corresponding to Model #2.

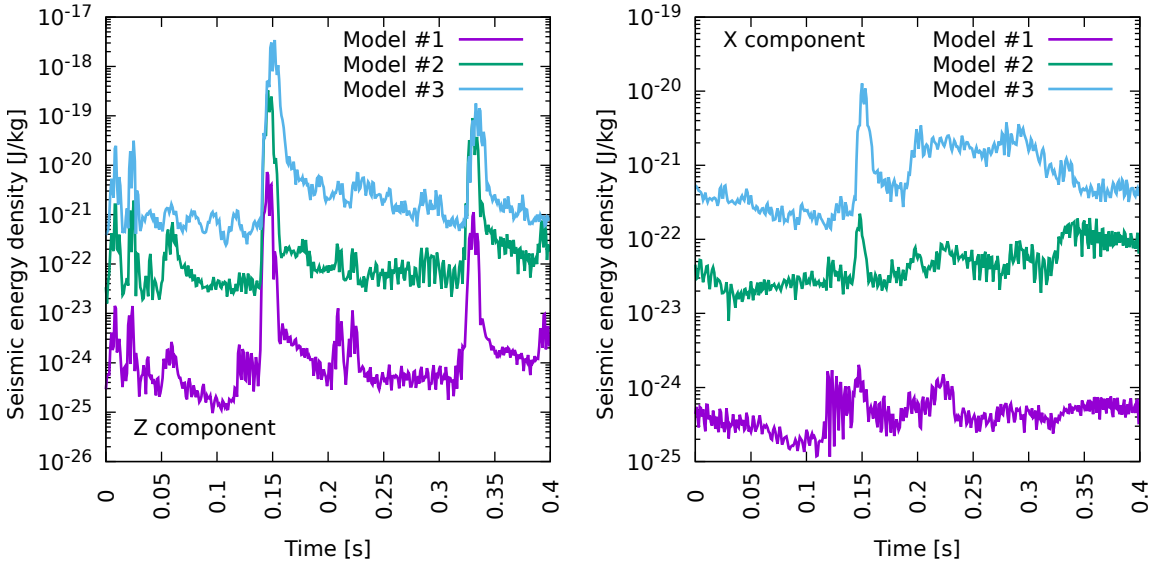

Figure 12. Comparison of the energy density of the surface seismic traces, considering the three different models. Each curve was obtained stacking the squared surface velocity traces recorded in all receivers, and dividing by the number of recorded traces.

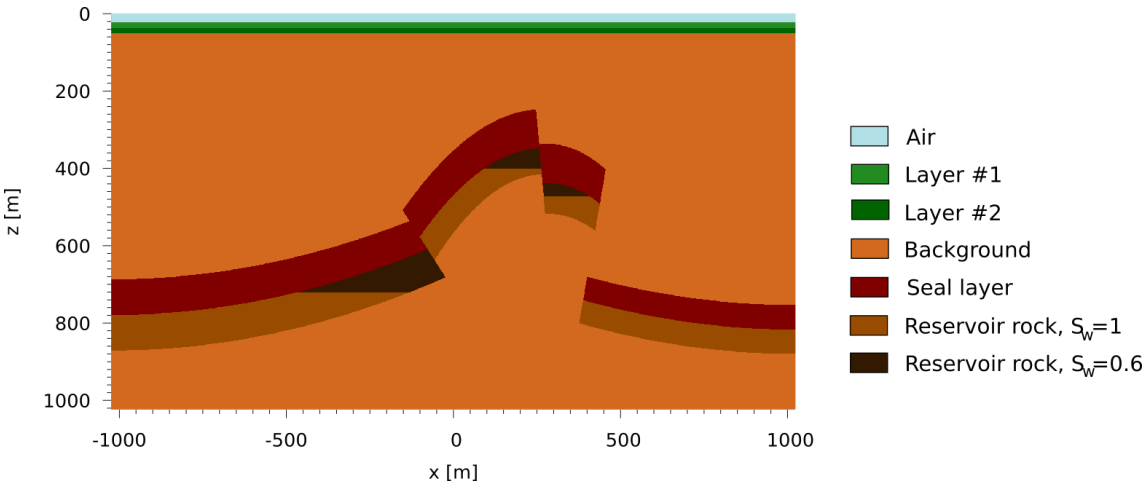

Figure 13. The different structures of this model have the same properties as the ones with the same colors in the previous three models. The water saturated reservoir rock, which is the only new one considered, has the following properties: $V_p = 2863$ m/s, $\sigma = 1.4 \times 10^{-3}$ S/m, $L_0 = 2.1 \times 10^{-10}$ A/(Pa m). One hundred receivers, from -800 m to 800 m separated 16 m from each other are located on the Earth's surface along the x-direction.

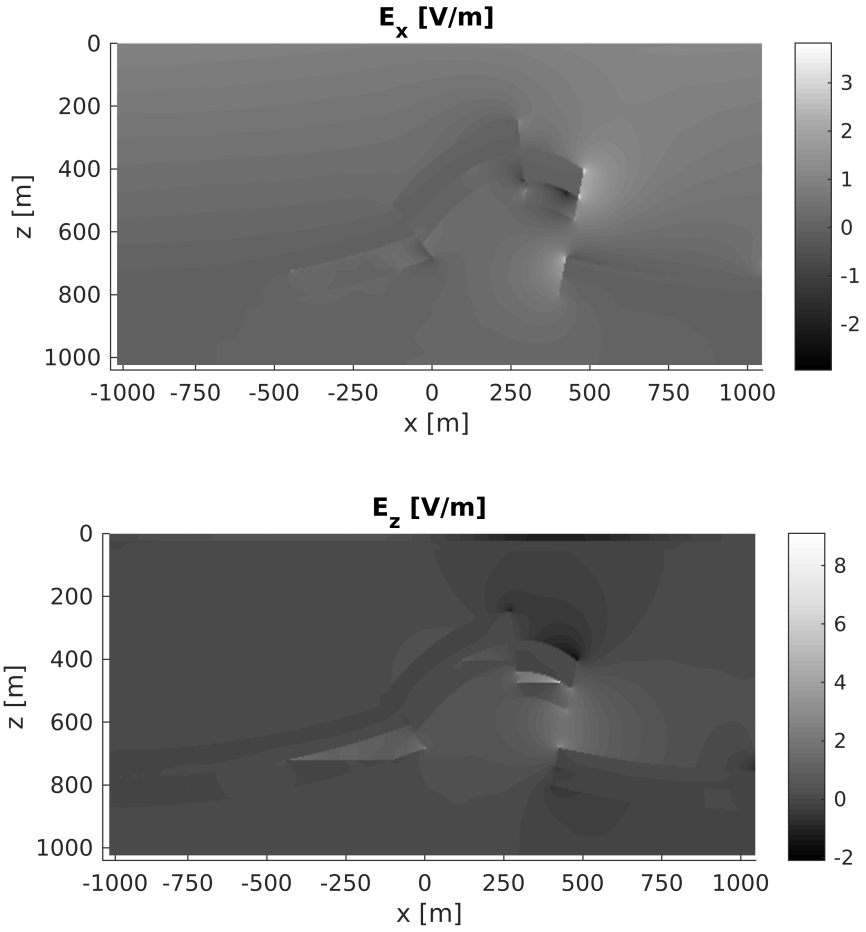

Figure 14. Electric field amplitudes (E_x top panel, E_z bottom panel), corresponding to a frequency of 120 Hz induced in the discussed model by the plane wave source field, arriving to the earth's surface with the same amplitude (1 V/m) as in the previous models.

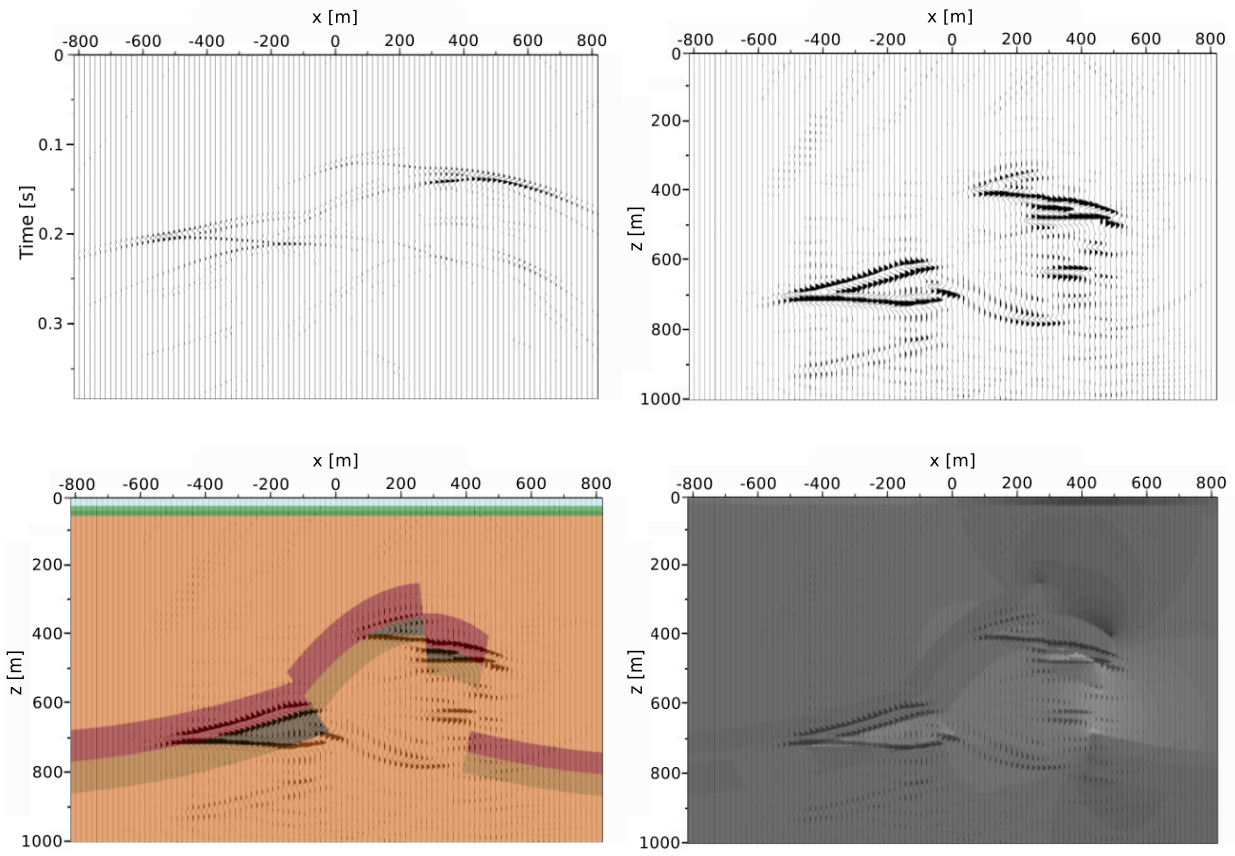

Figure 15. The top left panel depicts the z-component acceleration traces generated by the electroseismic conversion recorded at the surface. The top right panel is the depth migration of these traces. In the bottom panels we show how the migrated seismic data are agreement with the subsurface model and the vertical component of the electric field E_z.